IOSR Journal of Applied Chemistry (IOSR-JAC)
e-ISSN: 2278-5736.Volume 19, Issue 9 Ser. I (September. 2026), PP 06-33
www.iosrjournals.org

Novel Ruthenium(II) Coordination-Enhanced Cytotoxic Potency of Pyrazine-2-carbohydrazide Schiff Bases: Synthesis, Characterisation, In-vitro and Docking Studies

Shivaraj S Dolli[a], Laxmi A Jagatap[a], Ramesh Vadavi[a,] Tathagata Chakraborthy[b], Oruganti Anjaneyulu[b*], Kalagouda Gudasi[a,c**]

[a] *Dept. of Chemistry, Karnatak University, Dharwad, Karnataka, India.*
[b] *Dept. of Chemistry, Central University of Karnataka, Kalaburagi, Karnataka, India.*
[c] *Sri Jagadguru Murugharajendra University, Chitradurga, Karnataka, India.*

Abstract
Owing to their superior biocompatibility, tunable coordination chemistry, and selective accumulation in tumor tissues, ruthenium(II) complexes have emerged as potential competitors for platinum-based chemotherapy drugs. Building on the anticancer potential of pyrazine-2-carbohydrazide scaffolds, three novel Schiff base ligands (L1-L3) bearing electronically distinct imine-bound aryl substituents (4,4-dichlorobenzophenyl, 4-chlorobenzophenyl, and 2-aminobenzophenyl, respectively) were synthesised, together with their corresponding octahedral ruthenium(II) complexes [RuL1-RuL3] featuring bidentate N,N-coordination through the pyrazine and imine nitrogen donors. All compounds were characterised by $^{1}H/^{13}C$ NMR, FT-IR, UV-Visible, and mass spectrometry, while single-crystal X-ray diffraction of L1 and L3 (monoclinic, $P2_1/n$ and $P2_1/c$, respectively) unambiguously confirmed the ligand molecular structures. Cytotoxic evaluation against Caco-2 human colorectal adenocarcinoma cells by the MTT assay revealed concentration- and time-dependent antiproliferative effects, with IC_{50} values decreasing from 121.79–168.55 µg/mL (free ligands, 24 h) to 70.07–88.91 µg/mL (all compounds, 48 h). Ruthenium coordination markedly accelerated cytotoxic onset: at 24 h, RuL1 (IC_{50} = 106.26 µg/mL) and RuL3 (111.74 µg/mL) were the most potent, whereas by 48 h, RuL2 (70.07 µg/mL) and RuL3 (74.54 µg/mL) sustained superior activity, indicating ligand-dependent kinetics of action. Molecular docking of L1-L3 against EGFR (1M17), PI3Kα (4JPS), and Bcl-2 (4LXD) yielded binding energies of −8.1 to −8.9 kcal/mol, with ligand efficiency values of −0.33 to −0.36; interaction analysis showed that hydrogen-bonding and π-cation/π-stacking networks, rather than binding-pocket size, governed the affinity trends across targets, mirroring the substituent-dependent SAR observed in the cytotoxicity data. Collectively, these findings identify pyrazine-2-carbohydrazide-based ruthenium(II) complexes as multi-target-compatible scaffolds - engaging EGFR-, PI3Kα-, and Bcl-2-linked pathways — warranting further development as colorectal cancer therapeutics.

Keywords: *Ruthenium(II) complex; Pyrazine-2-carbohydrazide; in-vitro Anticancer; Insilico study;*

Date of Submission: 03-09-2026 Date of Acceptance: 13-09-2026

I. Introduction

Cancer continues to represent a major global health burden and remains one of the leading causes of mortality worldwide[1]. In 2022 alone, an estimated 20 million new cancer cases and 9.7 million cancer deaths were recorded globally, underscoring the scale of this challenge[1]. Despite significant advancements in diagnosis and treatment, chemotherapy remains a cornerstone in cancer management. Conventional platinum-based drugs such as cisplatin have demonstrated substantial clinical success; however, their long-term use is often associated with severe side effects including nephrotoxicity, neurotoxicity and myelosuppression and the development of drug resistance, thereby limiting their therapeutic efficiency[2,3]. These drawbacks have encouraged the search for alternative metal-based drugs with improved pharmacological profiles.

In recent decades, extensive research in the field of organometallic and coordination chemistry has led to the development of a wide range of metal complexes with diverse applications in catalysis, sensing, synthetic chemistry, energy conversion and medicinal chemistry[4–6]. Among these, organoruthenium compounds have attracted considerable attention due to their versatile chemical properties and broad spectrum of applications[7]. Ruthenium, a member of the iron group, exhibits favourable biological compatibility, contributing to its potential as a therapeutic agent, and can adopt multiple oxidation states, mainly Ru(II) and Ru(III) under physiological conditions, enabling diverse coordination chemistry[7]. In addition, ruthenium complexes generally exhibit low toxicity, selective accumulation in tumour tissues, and the ability to mimic iron binding to the plasma protein transferrin[7,8]. Because rapidly dividing tumour cells frequently overexpress transferrin receptors to meet their

elevated iron demand, this iron mimicking property promotes uptake and delivery of ruthenium complexes into cancer cells relative to the normal cells, thereby enhancing their potential as anticancer agents[8].

The biological performance of complexes is strongly influenced by the nature of the coordinating ligands. Minor modifications in the structural arrangement can lead to significant changes in activity. In this context, nitrogen-containing heterocycles have emerged as important scaffolds in ligand design. Pyrazine-2-carbohydrazide, a six-membered heterocyclic ring containing two nitrogen donor atoms, is widely recognised for its presence in numerous bioactive molecules reported to display antimicrobial, antifungal, anti-inflammatory, and anti-cancer activity[9]. In particular, the pyrazine scaffold is a promising framework in oncology drug design and appears in several clinically important anticancer agents at various stages of development (**Fig. 1**): Gliteritinib, a pyrazine carboxamide-based FLT3/AXL inhibitor, received FDA approval in 2018 for relapsed of refractory FLT3-mutated acute myeloid leukemia[10,11]; Radotinib, a pyrazine-pyrimidine benzamide Bcr-Ab1 inhibitor, has been approved in South Korea(KFDA) for chronic myeloid leukemia since 2012 but has not received FDA approval[12], and the pyrazine-2-carbonitrile/varboxamide derivatives Prexasertib (a CHK1/CHK2 inhibitor)[13] and Darovasertib currently holding FDA breakthrough-therapy and orphan-drug designation for uveal melanoma rather than full approval[14]. Building on these precedings, these pyrazine-2-carbohydrazide scaffolds have been extended further through their Schiff bases, which have also been extensively explored as ligands containing the azomethine (-CH=N-) functionality widely explored in coordination chemistry[15]. Since Schiff base complexation has itself been reportedly shown to enhance the biological activity of the parent ligand[16,17]. The Coordination of such ligands to ruthenium metal offers a rational strategy for synthesising complexes with enhanced pharmacological properties[18,19]. Combination of pyrazine-2-carbohydrazide frameworks with Schiff base functionality can further enrich ligand design by integrating multiple bioactive features into a single molecular system.

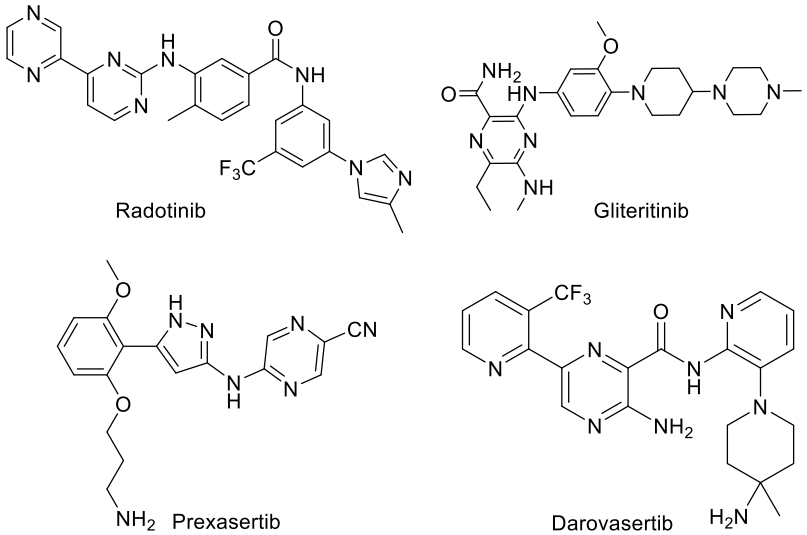

Fig. 1. Pyrazine containing anticancer agents at different statges of clinical development (Gilteritinib: FDA-approved; Radotinib: approved in South Korea; Prexasertib and Darovasertib: in clinical development).

An appropriate *in-vitr*o cancer cell models are crucial for examining the biological effectiveness of the newly synthesized Ru(II) complexes. Among the various *in-vitro* cancer models, the Caco-2 cell line derived from human colorectal adenocarcinoma epithelial cells has been widely employed to evaluate the anticancer potential and cytotoxicity[20]. Colorectal cancer (CRC) is among the most frequently diagnosed malignancies, accounting for an estimated 1.9 million new cases and over 900,000 deaths globally in 2022 alone[1], and continues to be a major cause of cancer-related deaths worldwide, highlighting the urgent need for improved therapeutic approaches[21]. Caco-2 cells possess the ability to differentiate into enterocyte-like monolayers exhibiting characteristic features such as tight junctions, brush border enzymes, and transporter proteins, thereby closely mimicking the intestinal epithelial barrier[21]. Owing to these properties, the Caco-2 model is extensively utilised for studying cellular uptake, drug permeability, and the biological interactions of metal-based chemotherapeutic agents[7]. Despite the demonstrated promise of Ru(II)-based anticancer agents and the well-established bioactivity of pyrazine-2-carbohydrazide Schiff bases bearing systematically varied substituents, they remain largely unexplored for their cytotoxicity against colorectal cancer.

Based on these considerations, the present research focuses on the design and synthesis of novel pyrazine-2-carbohydrazide derivatives and their organoruthenium complexes, and the comparative evaluation of their anticancer activity as bare ligands verses ruthenium complexes against the Caco-2 cell line using MTT cytotoxicity assay.

II. Experimental Section

Materials and Methods

All chemicals employed in this study were obtained from commercial sources as Analytical Research Grade (AR Grade) and were used without extra purification. The melting points of the newly synthesised scaffolds have been determined and are reported as uncorrected values. The purity of the compounds was assessed by thin-layer chromatography (TLC) using silica gel plates (silica gel 60 F254, Merck). Infrared spectra were recorded on a PerkinElmer FT-IR instrument. Proton and carbon NMR spectra have been acquired in $CDCl_3$ or DMSO-d_6 as solvent using Bruker 600 MHz instrument, with chemical shifts reported in parts per million (ppm) relative to tetramethyl silane (TMS) as an internal standard. UV-Visible spectra were conducted through a Thermo Scientific Genesys 150 instrument. Mass spectra have been obtained on a Thermo Fisher HRMS instrument.

Synthesis of Pyrazine-2-carbohydrazide (PyHy)

PyHy was synthesised as illustrated in **Scheme 1**. To a cold methanolic solution of Pyrazine-2-carboxylic acid (64 mmol, 20 mL), concentrated sulphuric acid (30 mol%, 1.7 mL) is added dropwise with constant stirring. The reaction mixture was refluxed for 16 hrs, and the progress of the reaction was monitored using TLC. Methanol is evaporated under reduced pressure. Sulphuric acid was neutralised by sodium bicarbonate solution, then extracted with ethyl acetate, the solvent was removed on a rotavapor to obtain methyl pyrazine-2-carboxylate[9].

Methyl pyrazine-2-carboxylate (1 mol) was dissolved in methanol and refluxed with hydrazine hydrate (2.5 eq) for 2 h, until precipitation occurred. The precipitate is filtered and washed with cold methanol to yield pyrazine-2-carbohydrazide.

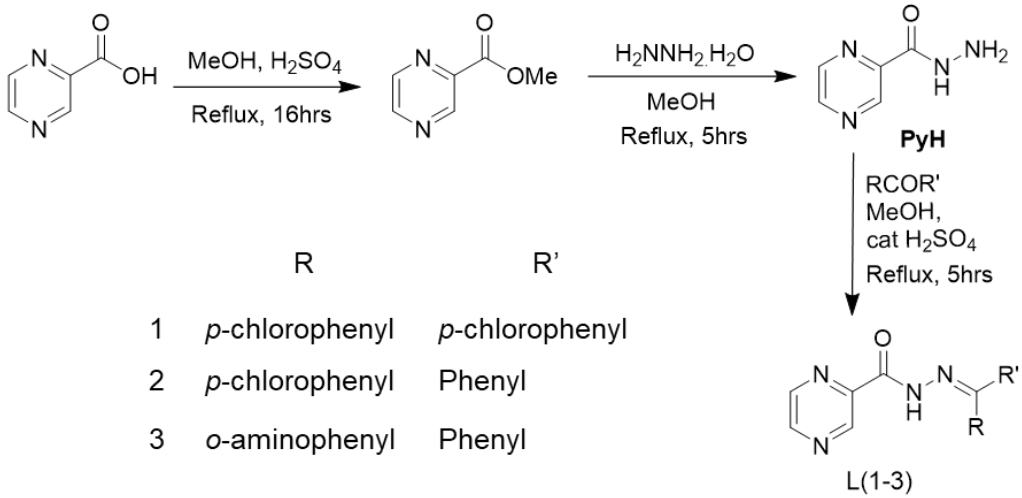

Scheme 1: Synthesis of diphenyl methyl pyrazine-2-carbohydrazide derivatives L1-L3.

General Synthesis of ligands diphenyl methyl pyrazine-2-carbohydrazide derivatives L1-L3

The ligands L1-L3 were synthesised as illustrated in **Scheme 1**. To a methanolic solution of pyrazine-2-carbohydrazide (1 mmol), substituted aromatic ketones (1 eq.) were added in the presence of a catalytic quantity of concentrated sulphuric acid. The reaction mixture was refluxed for 5 hours to get precipitate. The precipitate was filtered and washed with hot methanol to yield pure pyrazine-2-carbohydrazide derivatives.

L1 : N'-(bis(4-chlorophenyl)methylene)pyrazine-2-carbohydrazide

Yield.69%; Pale Yellow solid; m.p. 214-216 ^oC; IR υ max (cm^{-1}). 3320, 3086, 1686, 1483, 1090, 835; ^1H NMR (600 MHz, $CDCl_3$) δ 10.60 (s, 1H), 9.46 (s, 1H), 8.74 (d, J = 2.0 Hz, 1H), 8.38 (d, J = 2.3 Hz, 1H), 7.62 (d, J = 8.0 Hz, 4H), 7.35 - 7.32 (d, 2H), 7.32 - 7.30 (d, 2H); ^{13}C NMR (151 MHz, $CDCl_3$) δ 158.67, 154.13, 147.76, 144.93, 143.84, 142.57, 136.56, 134.95, 130.25, 129.42, 128.68. LCMS Observed mass $[M]^+$ m/z 371.05; Calculated mass. 371.22; CHN analysis for $C_{18}H_{12}Cl_2N_4O$ Calcd. C, 58.24; H, 3.26; Cl, 19.10; N, 15.09; O, 4.31;

L2 : N'-((4-chlorophenyl)(phenyl)methylene)pyrazine-2-carbohydrazide

Yield.82%; White solid; m.p. 186-188 ^oC; IR υ max (cm^{-1}). 3309, 3085, 1684, 1485, 1088, 840; ^1H NMR (600 MHz, $CDCl_3$) δ 10.65 (s, 1H), 9.46 (s, 1H), 8.70 (d, J = 2.2 Hz, 1H), 8.32 (d, J = 2.2 Hz, 1H), 7.67 - 7.62 (m, 5H), 7.35 - 7.33 (m, 4H); ^{13}C NMR (151 MHz, $CDCl_3$) δ 158.65, 155.47, 147.58, 144.90, 144.03, 142.48, 136.42, 135.24, 131.55, 130.28, 129.84, 129.52, 128.57, 128.35; LCMS Observed mass $[M+H]^+$ m/z 337.07; Calculated mass. 336.78; CHN analysis for $C_{18}H_{13}ClN_4O$ Calcd. C, 64.20; H, 3.89; Cl, 10.53; N, 16.64; O, 4.75;

L3 : N'-((2-aminophenyl)(phenyl)methylene)pyrazine-2-carbohydrazide

Yield.69%; Yellow solid; m.p. 248-250 °C; IR υ max (cm^{-1}). 3312, 3296, 3053, 1697, 1510, 1485, 1021, 835; ^{1}H NMR (600 MHz, DMSO) δ 10.68 (s, 1H), 9.29 (s, 1H), 8.88 (d, *J* = 2.1 Hz, 1H), 8.60 – 8.56 (d, 1H), 7.67 – 7.62 (m, 2H), 7.45 (d, *J* = 5.7 Hz, 3H), 7.31 (t, *J* = 7.8 Hz, 1H), 6.94 (dd, *J* = 7.8, 5.2 Hz, 2H), 6.76 (t, *J* = 7.4 Hz, 1H); ^{13}C NMR (151 MHz, DMSO) δ 158.59, 155.20, 148.75, 145.98, 144.24, 144.08, 143.89, 136.88, 131.51, 130.49, 129.43, 128.94, 128.09, 117.18, 116.43, 114.97; LCMS Observed mass $[M-H]^+$ m/z 316.32; Calculated mass. 317.23; CHN analysis for $C_{18}H_{12}Cl_2N_4O$ Calcd. C, 68.13; H, 4.76; N, 22.07; O, 5.04;

Synthesis of Ruthenium(II) Complexes

Metal complexes were synthesised according to the previously established method[22]. Initially, $Ru(PPh_3)_3Cl_2$ is dissolved in 2 mL DCM under nitrogen, then stoichiometric ratio (1:1 or 1:2) of the ligand is dissolved in 5 mL DCM separately. Ligand was injected through syringe and the reaction mixture was refluxed at 45 ^{0}C with constant stirring under nitrogen atmosphere for 4-6 h. The reaction mixture was cooled to ambient temperature and hexane/diethyl ether was added with constant stirring to initiate the precipitate, and kept in refrigerator to increase the precipitation. The formed precipitate was filtered, washed with excess diethyl ether and the obtained solid was dried and stored in desiccators over $CaCl_2$ at ambient temperature.

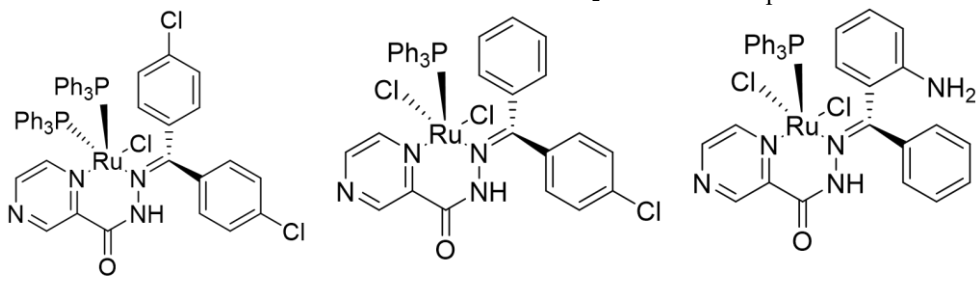

Fig. 2. Plausible structures of complexes RuL1, RuL2 and RuL3.

RuL1

Yield 65%; Black solid; m.p.. >250 °C; IR υ max (cm^{-1}). 3296, 3056, 1702, 1515, 1091, 838, 695, 518, 499; ^{1}H NMR (600 MHz, DMSO) δ 10.61 (s, 1H), 9.27 (s, 1H), 8.88 (s, 1H), 8.61 (s, 1H), 7.78 (d, *J* = 7.1 Hz, 5H), 7.56 (t, *J* = 9.5 Hz, 8H), 7.41 (d, *J* = 3.8 Hz, 12H), 7.26 - 7.23 (m, 7H). ^{13}C NMR (151 MHz, DMSO) δ 158.28, 153.36, 148.34, 143.43, 136.59, 133.17, 131.50, 131.43, 131.19, 130.51, 129.97, 129.22, 128.98, 128.78, 128.74, 127.61; LCMS Observed mass $[M+H]^+$ m/z 1031.99; Calculated mass. 1031.09; CHN analysis for $C_{54}H_{42}Cl_3N_4OP_2Ru$ Calcd. C, 62.83; H, 4.10; Cl, 10.30; N, 5.43; O, 1.55; P, 6.00; Ru, 9.79.

RuL2

Yield 78%; Muddy Brown solid; m.p.. >250 °C; IR υ max (cm^{-1}). 3299, 3058, 1694, 1508, 1090, 693, 519, 497; ^{1}H NMR (600 MHz, DMSO) δ 10.66 (s, 1H), 9.33 (s, 1H), 8.93 (s, 1H), 8.60 (s, 1H), 7.76 (d, *J* = 7.1 Hz, 4H), 7.64 - 7.59 (m, 5H), 7.46 (d, *J* = 4.0 Hz, 9H), 7.33 - 7.27 (m, 6H); ^{13}C NMR (151 MHz, DMSO) δ 158.77, 153.85, 148.83, 144.27, 143.92, 137.15, 137.08, 133.79, 133.66, 131.99, 131.68, 131.00, 130.46, 129.71, 129.47, 129.27, 129.23, 128.23, 128.10; LCMS Observed mass $[M-Cl-PPh_3]^+$ m/z 487.25; Calculated mass. 770.01; CHN analysis for $C_{36}H_{28}Cl_3N_4OPRu$ Calcd. C, 58.78; H, 3.84; Cl, 9.64; N, 7.62; O, 2.17; P, 4.21; Ru, 13.74.

RuL3

Yield 57%; Dark Brown solid; m.p.. >250 °C; IR υ max (cm^{-1}). 3303, 2960, 1874, 1434, 1091, 671, 519, 498; ^{1}H NMR (600 MHz, DMSO) δ 10.67 (s, 1H), 9.33 (s, 1H), 8.94 (d, *J* = 2.7 Hz, 1H), 8.67 (d, *J* = 2.0 Hz, 1H), 7.82 (d, *J* = 8.1 Hz, 1H), 7.68 (dd, *J* = 13.0, 6.3 Hz, 4H), 7.62 (d, *J* = 2.4 Hz, 2H), 7.61 – 7.57 (m, 4H), 7.47 (d, *J* = 3.9 Hz, 9H), 7.33 – 7.29 (m, 6H); ^{13}C NMR (151 MHz, DMSO) δ 157.34, 152.43, 147.40, 142.49, 135.65, 132.23, 130.56, 130.50, 130.25, 129.57, 129.03, 128.28, 128.04, 127.85, 127.80; LCMS Observed mass $[M-2H-PPh_3]^+$ m/z 486.94; Calculated mass. 751.06; CHN analysis for $C_{36}H_{30}Cl_2N_5OPRu$ Calcd C, 57.53; H, 4.02; Cl, 9.43; N, 9.32; O, 2.13; P, 4.12; Ru, 13.45.

X-Ray Crystallography

Single rectangular crystal of L1 was mounted on a suitable support on an XtaLAB Synergy, Dualflex, HyPix diffractometer. The crystal was kept at a steady *T* = 293(2) K during data collection. The structure was solved with ShelXT 2018/2 [23] and **Olex2** [24] as the graphical interface. The model was refined with version 2025/1 of ShelXL 2025/1 using least-squares minimisation.

Anticancer activity (*MTT assay)*

The cytotoxicity of test compounds was assessed using the MTT assay. Initially, cells were plated in a 96-well format at a density of 20,000 cells per well and incubated for 24 hours at 37°C with 5% CO_2 to achieve approximately 80% confluence. After incubation, cells were treated with varying concentrations of the test compounds for an additional 24 hours. After the treatment, the culture medium was removed, and 10 µL of MTT reagent alongside 100 µL of fresh DMEM medium were added to each well, with further incubation at 37°C for 4 hours[25]. This allows metabolically active cells to convert the yellow MTT into insoluble purple formazan crystals. After incubation, the MTT medium was discarded, and 150 µL of dimethyl sulfoxide (DMSO) was added to dissolve the formazan crystals; the plate was then gently shaken for complete solubilization. Absorbance was measured at 570 nm using a microplate reader, and cell viability was calculated by comparing the absorbance of treated cells with untreated controls using equation 1, expressed as a percentage of viable cells.

$$Cell\ viability\ (\%) = \frac{Mean\ O.D\ of\ test\ sample}{Mean\ O.\ D\ of\ control} \times 100 \qquad (1)$$

Molecular docking study

Molecular docking was performed to investigate the behaviour of synthesised ligands toward selected biologically relevant protein targets and to identify the principal non-covalent interactions governing ligand recognition. The target proteins were selected based on their established involvement in cancer-associated signalling and survival pathways, namely epidermal growth factor receptor (EGFR; PDB ID: 1M17), phosphatidylinositol-3-kinase alpha (PI3Kα; PDB ID: 4JPS), and B-cell lymphoma 2 protein (Bcl-2; PDB ID: 4LXD). EGFR is a clinically important tyrosine kinase implicated in tumour cell proliferation and survival, PI3Kα is a major component of the PI3K/AKT signalling axis frequently associated with oncogenic growth and metabolic regulation, and Bcl-2 is a key anti-apoptotic protein that supports cancer cell survival by suppressing programmed cell death.

The three-dimensional structures of the ligands were generated and geometry-optimised using Avogadro, employing the MMFF94 force field to obtain energetically favourable conformations prior to docking. The optimised ligand structures were subsequently prepared in AutoDockTools (ADT) [26]by assigning the appropriate atom types, charges, and torsional parameters required for docking calculations[27].

The crystallographic structures of the target proteins were retrieved from the Protein Data Bank and assessed for structural reliability before docking. Protein quality was verified by PROCHECK through Ramachandran plot analysis to confirm acceptable stereochemical geometry. During receptor preparation, co-crystallised ligands, solvent molecules, and other heteroatoms not directly involved in docking were removed, polar hydrogens were added, and Kollman and Gasteiger charges were assigned using ADT[26].

Docking simulations were carried out using AutoDock Vina[28]. For each target, the grid box was centered on the active-site region and defined with dimensions of 40 Å × 40 Å × 40 Å to ensure adequate coverage of the binding cavity. Ten binding poses were generated for each ligand under an energy range of 4, and each docking experiment was repeated in five independent runs to evaluate the reproducibility and consistency of the predicted binding orientations[29].

Ligand efficiency (LE) approach

LE was employed to assess the binding performance of the synthesised ligands relative to their molecular size[30]. The calculation was derived from the dissociation constant K_d of the ligand-protein complex, which serves as an indicator of binding affinity[31]. Lower K_d values correspond to stronger ligand-receptor interaction and greater complex stability. The relationship between the binding free energy (ΔG^0 and K_d was determined using the following equations **(2)** and **(3).**

ΔG^0 = -2.303RTlog(K_d) **(2)**

$K_d = 10^{\frac{\Delta G^0}{2.303RT}}$ **(3)**

Where ΔG^0 (kcal/mol) represents binding energy obtained from molecular docking studies, R is the universal gas constant in kcal, T is absolute temperature in Kelvin (298.15 K). To compare compounds of different molecular sizes, ligand efficiency was calculated by normalising the binding free energy with respect to heavy atom count (HAC), as shown in Equation **(4)**.

$LE = -\frac{2.303RT}{HAC}\log(K_d)$ **(4)**

The LE parameter provides an estimate of the binding contribution per heavy atom and is widely used to evaluate the quality of the ligand target interactions during lead optimisation studies.

III. Results and Discussion

Synthesis and Structural Characterisation

All the target pyrazine-2-carbohydrazide derivatives and their Ru(II) complexes were prepared in moderate to excellent yield. The structural and coordination features of the synthesised pyrazine-2-carbohydrazide-based ligands (L1-L3) and their respective Ru(II) complexes were studied using several spectroscopic techniques.

NMR Spectra

The ^{1}H NMR spectra of ligands L1-L3 exhibited characteristic singlets for the amide hydrogen(-NH) proton at δ 10.6 ppm, and one singlet and two doublet peaks at δ 9.4, δ 8.7, and δ 8.3 ppm respectively, from the pyrazine ring. Multiplet signals are observed between δ 6.75 - 7.75 ppm are attributed to aromatic ring protons of benzophenone ring. In ligand L3, 2H singlet corresponds to the -NH_2 proton. Upon coordination with Ruthenium, there is no shift in the amide proton signal, indicating the -NH has not participated in the complexation. The three protons from the pyrazine ring showed an upfield shift relative to the bare ligands reflects that the pyrazine-N as one of the donar atoms. The Presence of new peaks in the region of δ 7.25-7.75 ppm corresponds to the 15 hydrogens present in the triphenylphoshine ring. The NMR data can be found in the supplementary data.

FT-IR Spectra

The infrared spectra of the bare ligands L1-L3 exhibited characteristic absorption bands corresponding to their functional groups **(Table 1)**. A band in the region 3320-3296 cm^{-1} corresponds to ν(-NH) stretching. While bands at 3086-3053 cm^{-1} assigned to aromatic ν(C-H) stretching. The strong absorption band observed at 1697-1684 cm^{-1} is attributed to carbonyl ν(C=O) stretching, Bands in the regions 1591-1485 cm^{-1}, 1145-1021 cm^{-1} are assigned to ν(C=N) and ν(C=C) vibrations respectively. Upon complexation with Ru(II), the ν(C=O) band shifted to 1874-1694 cm^{-1}, indicating carbonyl is not associating in the coordination.. Shifts in ν(C=N) band, along with new bands in the region around 519 cm^{-1}, is attributed to the formation of (Ru-N) bond. These findings suggest the involvement of nitrogen in metal binding, supporting bidentate N,N-chelation. FT-IR spectra of the above compounds are given in the supplementary data.

Table 1. FTIR spectra of compounds L1-Ru(L3).

Compounds	Frequency (cm^{-1})					
	ν(N-H)	ν(C-H) aromatic	ν(C=O) (amide)	ν(C=N) azomethine	ν(N-N)	ν(Ru-N)
L1	3320	3086	1686	1591	1145	--
RuL1	3296	3056	1702	1515	1091	518,499
L2	3309	3085	1684	1485	1088	--
RuL2	3299	3058	1694	1508	1090	519,497
L3	3312, 3296	3053	1697	1510	1021	--
RuL3	3303	2960	1874	1434	1090	519,498

UV-Visible spectra

The UV-Vis spectra of the pyrazine-2-cabohydrazide ligands (L1-L3) were carried out in dimethylformamide (DMF) at a concentration of 1.0 x 10^{-4} M using a 1 cm path length quartz cuvette[32]. Intense absorption bands at 270 nm are attributed to ligand-centered π→π* transitions of the aromatic system, while bands in the 306-318 nm region correspond to n→π* transitions involving lone-pair electrons of the heteroatom-containing functionalities. Upon Ruthenium(II) coordination. New broad absorption bands in the 384-486 nm region are observed for RuL1-RuL3**(Table 2)**, which are not appeared in the bare ligands. These lower-energy absorption bands are attributed to Ligand-Metal Charge Transfer(LMCT)/Metal-Ligand Charge Transfer(MLCT) transitions. These characteristics provides evidence for complexation of the hydrazone ligand to the Ru(II) center through its donor nitrogen atom (**Fig. S25)**.

Table 2. UV-Vis. Spectral data of compounds L1 to RuL3.

Compounds	Wavelength(nm)		
	π→π*	n→π*	MLCT/LMCT
L1	270	318	--
RuL1	270	--	486
L2	270	314	--
RuL2	270	316	421
L3	270	306	--
RuL3	270	--	384

Mass Spectrometry

The molecular ion peak of L1 with m/z value 371.05 $[M]^+$, L2 with m/z value 337.07 $[M+H]^+$ and L2 with m/z value 316.32 $[M-H]^+$ which are in line with the molecular weight of the ligands as evidenced in supplementary data**.** The molecular ion peak of Ruhenium(II) complexes namely RuL1 1031$[M+H]^+$, RuL2 487$[M\text{-}Cl\text{-}PPh_3]^+$ and RuL3 486.9$[M\text{-}PPh_3]^+$ were assigned based on their mass-to-charge ratio[33]. These values agree well with the proposed composition of the complexes as shown in the **Fig. 2**. Hence, the mass studies confirm the formation of the complexes.

X-Ray Crystallography

Both ligands L1 and L3 were crystallised using the slow evaporation method with a chloroform-ethanol mixture. The molecular structure of the ligand was unambiguously established by single crystal X-ray diffraction analysis. Both ligands crystallised in the monoclinic crystal system with the centrosymmetric $P2_1/n$ and $P2_1/c$ respectively. The crystallographic data are shown in **Table 3.** This confirms the ligand structures and crystallographic properties. The ORTEP diagrams are illustrated in Fig.3. The other details, like bond angles and bond lengths, were given in **Table S1-S4**.

Table 3. Crystal data of ligands L1 and L3.

Compound	**L1**	**L3**
CCDC number	2580315	2584807
Formula	$C_{18}H_{12}Cl_2N_4O$	$C_{18}H_{15}N_5O$
$D_{calc.}$/ g cm^{-3}	1.413	1.303
μ /mm^{-1}	3.461	0.692
Formula Weight	371.22	317.35
Colour	Pale Yellow	Yellow
Shape	Rectangular	rectangular
T/K	293(2)	293(2)
Crystal System	monoclinic	monoclinic
Space Group	$P2_1/n$	$P2_1/c$
a/Å	10.6543(2)	6.8463(1)
b/Å	13.4158(3)	16.0804(3)
c/Å	12.3381(3)	14.8496(2)
a/°	90	90
b/°	98.253(2)	98.256(2)
g/°	90	90
V/Å^3	1745.29(7)	1617.87(4)
Z	4	4
Z'	1	1
Wavelength/Å	1.54184	1.54184
Radiation type	CuK_a	CuK_a
Q_{min}/°	4.897	4.08
Q_{max}/°	67.064	67.063
Measured Refl.	15996	14803
Independent Refl.	3119	2884
Reflections with I > 2(I)	2647	2638
R_{int}	0.0464	0.0219
Parameters	227	222
Restraints	0	0
Largest Peak	0.515	0.468
Deepest Hole	-0.409	-0.460
GooF	1.087	1.044
wR_2 (all data)	0.1568	0.1428
wR_2	0.1498	0.1400
R_1 (all data)	0.0541	0.0529
R_1	0.0477	0.0502

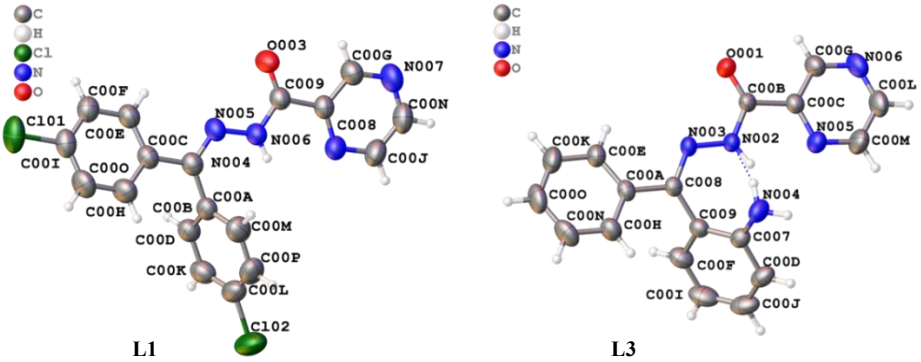

Fig. 3. ORTEP diagram of the ligands L1 and L3 illustrated Respectively.

***Anticancer activity** (MTT assay)*

The cytotoxic activity of the pyrazine-2-carbohydrazide Schiff base ligands (L1-L3) and their corresponding ruthenium complexes (RuL1-RuL3) was evaluated against the Caco-2 human colorectal adenocarcinoma cell line by the MTT assay, at concentrations of 5, 10, 25, 50 and 100 µg/mL over 24 and 48 h of exposure. As displayed in **Fig. 4**, all six compounds produced a clear concentration-dependent decline in Caco-2 cell viability: at the lowest dose (5 µg/mL) viability remained close to that of untreated controls (≥98% at 24 h), whereas at the highest dose (100 µg/mL) viability fell to approximately 55-61% at 24 h and further to 44-53% at 48 h. The decrease in viability was also time-dependent, with all compounds showing lower cell survival after 48 h than after 24 h at the same concentration, confirming a progressive and sustained antiproliferative effect rather than a transient one. The relative potency of the compounds was quantified in terms of their IC_{50} values, summarised in **Table 4.**

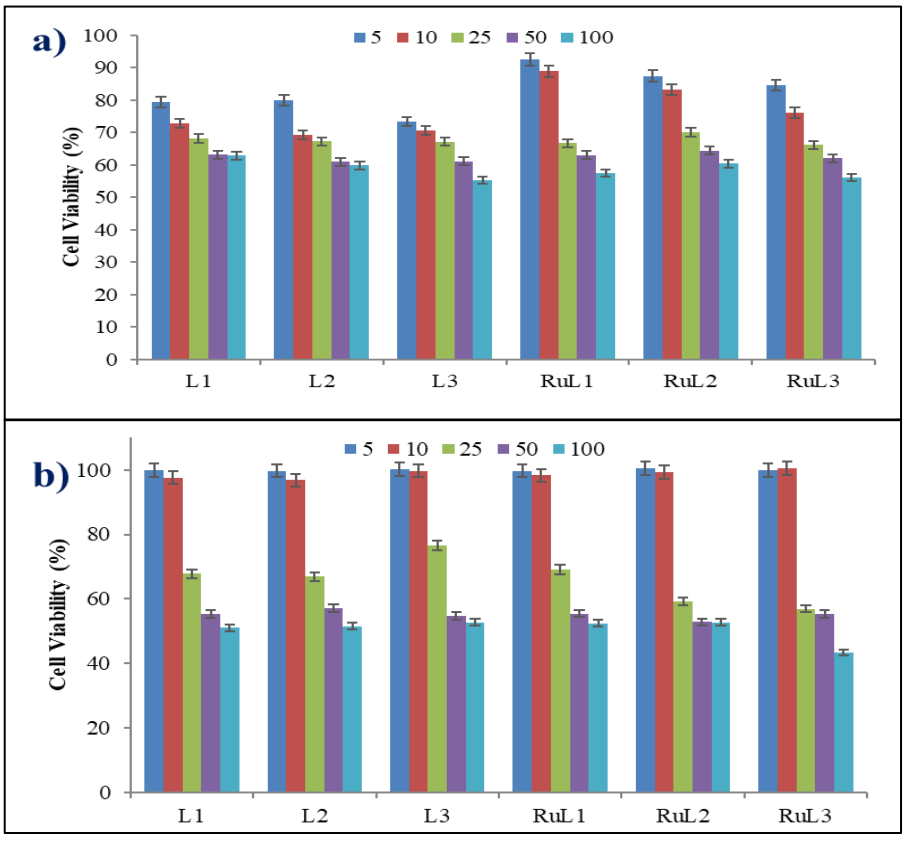

FIG. 4. Cell viability of Ligands L1-L3 and complexes RuL1-Rul3 **a)** 24 hrs **b)** 48 hrs.

The cytotoxic potency of the bare ligands at 24 h was observed to follow the order L3 > L2 > L1, as indicated by the decreasing IC50 values from 168.55 µg/mL (L1) to 142.64 µg/mL (L2) and 121.79 µg/mL (L3). This trend is attributable to the electronic nature of the substituents present on the imine-bound phenyl ring. Specifically, the substitution of one electron-withdrawing 4,4-dichlorophenyl group in L1 with 4-chlorophenyl

ring in L2, and further replacement with a 2-aminobenzophenyl group containing an electron-donating and hydrogen-bonding -NH_2 substituent in L3, resulted in a progressive enhancement of cytotoxic activity. These findings indicate that a decrease in the overall electron-withdrawing character, combined with the increased donor and acceptor capacity provided by the free amino group, facilitates more effective interactions with intracellular biomolecular targets.

Table 4. Cell viability and IC_{50} values (µg/mL) of ligands L1-L3 and ruthenium complexes RuL1-RuL3 against Caco-2 cells at 24 and 48 h

Sl. No	Compounds	Cell viability (IC_{50} value)	
		for 24 h	**for 48 h**
1	**L1**	168.55	85.49
2	**L2**	142.64	87.06
3	**L3**	121.79	88.91
4	**RuL1**	106.257	87.75
5	**RuL2**	124.53	70.07
6	**RuL3**	111.74	74.54

The coordination of the ligands to ruthenium significantly affected cytotoxic potency in a time-dependent manner. At 24 h, all ruthenium complexes exhibited greater cytotoxicity compared to their respective parent ligands. Notably, RuL1 (IC50 = 106.26 µg/mL) demonstrated an increase in potency of nearly 60 µg/mL relative to L1 (168.55 µg/mL), representing the most active compound at this time point, with RuL3 (111.74 µg/mL) displaying comparable activity. The pronounced enhancement in cytotoxicity upon metalation is consistent with established findings for ruthenium(II) anticancer complexes, where coordination is known to increase lipophilicity and promote cellular uptake. Furthermore, the presence of the metal centre enables additional interactions with cellular biomolecules, such as DNA or protein donor atoms, which are not accessible to the free organic ligands.

At 48 h, the difference in cytotoxic potency between the ligands and their corresponding ruthenium complexes was substantially reduced, resulting in a change in the activity ranking. RuL2 (70.07 µg/mL) and RuL3 (74.54 µg/mL) were identified as the most potent compounds, while RuL1 (87.75 µg/mL) exhibited a potency similar to its parent ligand L1 (85.49 µg/mL). It was observed that L1 displayed the greatest improvement in potency between 24 and 48 h, with its IC50 value nearly halved, whereas RuL1 showed minimal change over the same period. This indicates that RuL1 achieves its maximal cytotoxic effect rapidly, within 24 h, whereas L1 requires a longer duration to reach comparable efficacy. Collectively, these findings demonstrate that ruthenium coordination accelerates the onset of cytotoxicity, and this effect is sustained with prolonged exposure for the L2- and L3-derived complexes. Therefore, RuL2 and RuL3 are identified as the most promising candidates for further mechanistic studies and *in-vivo* evaluation.

Overall, the results of the MTT assay demonstrate that the synthesised pyrazine-2-carbohydrazide Schiff base ligands and their ruthenium complexes exhibit concentration- and time-dependent antiproliferative activity against Caco-2 cells. The cytotoxic potency can be modulated by varying the imine substituent and through metal coordination, with the amino-substituted and ruthenium-coordinated derivatives displaying the most significant therapeutic potential.

Insilco studies

Molecular docking studies were performed for the ligands L1-L3 against the targets EGFR(1M17), PI3Kα(4JPS), and Bcl-2(4LXD). The interaction profiles were systematically evaluated based on binding energy, predicted dissociation constant (K_d), LE, and interactions as obtained from the interaction table (**Table S5-S7**). The docking outcomes were interpreted by correlating the numerical affinity values with the nature and extent of non-covalent interactions, such as Hydrogen bonding, electrostatic interactions, and hydrophobic interactions, in accordance with established molecular docking analysis protocols.

Every ligands exhibited favourable predicted binding affinities across the protein targets, with binding energies ranging from -8.1 to -8.9 kcal/mol and LE values consistently between -0.33 and -0.36. These findings suggest that the ligands possess comparable atom-wise binding efficiency. Although the difference in binding energies are modest, the interaction profiles reveal ligand-dependent variation in the contribution of non-covalent interactions, thereby providing a mechanistic explanation for the observed trends in affinity.

EGFR interactions

Against EGFR, the ligands showed the affinity order L3 (-8.7 kcal/mol) > L1 (-8.6 kcal/mol) > L2 (-8.4 kcal/mol), with corresponding K_d values of 4.17 x 10^{-7} M, 4.94 x 10^{-7} M, 6.92 x 10^{-7} M, respectively. The LE values remained close for all three compounds (-0.36, -0.34, and -0.35 respectively), indicating that the improved affinity of L3 arises from a more favourable interaction pattern rather than a major difference in size-normalised efficiency.

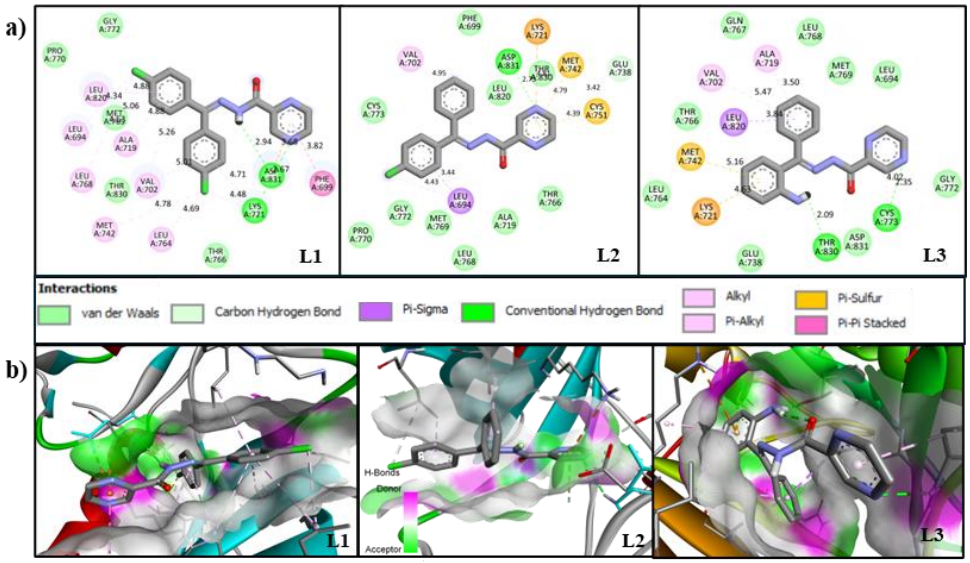

Fig. 5. a) 2D and b) 3D docking images of ligands L1-L3 with *EGFR (1M17)*

Docking Studies against EGFR demonstrated distinct binding interactions for each ligand as shown in **Fig. 5**. L1 was established by one conventional hydrogen bond and two π-anion contacts with ASP831, a π-π stacking interaction with PHE699, and extensive alkyl/π-alkyl interactions involving LEU694, LEU768, LYS721, MET742, LEU764, VAL702, ALA719, and LEU820. L2 exhibited a conventional hydrogen bond with ASP831 (HN1-N3) and a carbon-hydrogen bond with GLU738, a π-sigma interaction with LEU694 and VAL702. The comparatively narrower hydrophobic network of L2, relative to L1 and L3, is likely responsible for its reduced binding energy. L3 displayed the most favourable docking score, forming two conventional hydrogen bonds (CYS773, THR830), a π-cation interaction with LYS773, LYS721, VAL702, and ALA719. The presence of dual hydrogen-bond anchoring, together with dense hydrophobic and electrostatic interactions, accounts for the superior binding affinity of L3 compared to L1 and L2.

PI3Kα interactions

Docking against PI3Kα exhibited an affinity order L3(-8.6 kcal/mol) > L2 (-8.5 kcal/mol) > L1 (-8.2 kcal/mol), while the LE follows the same order with values -33, -35, -36 respectively. The corresponding K_d values reported in the interaction table were 4.94 x 10^{-7} M for L3, 5.85 x 10^{-7} M for L2, and 9.7 x 10^{-7} M for L1, supporting the same rank order of predicted affinity.

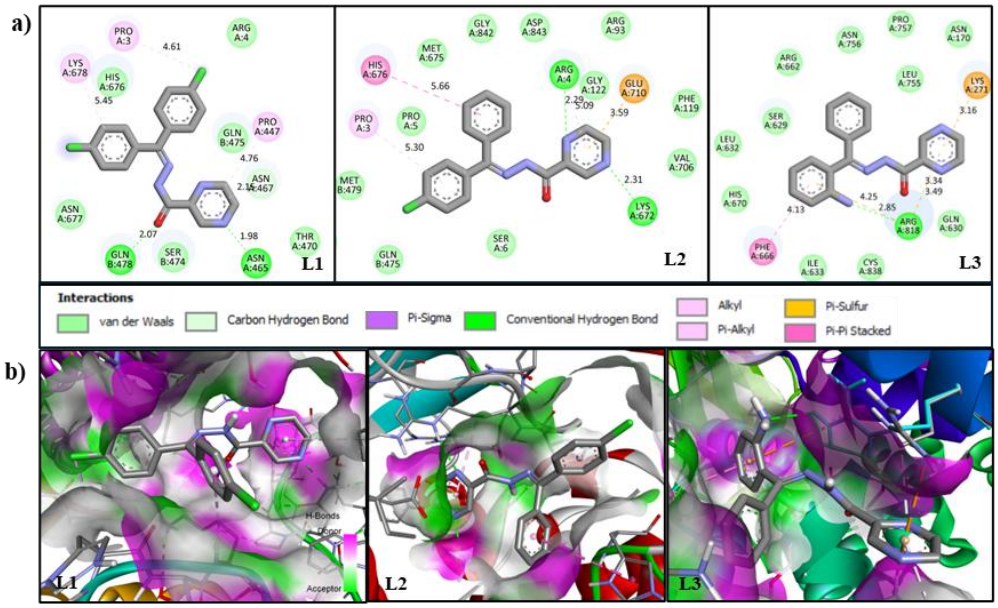

Fig. 6. a) 2D and b) 3D docking images of ligands L1-L3 with *PI3Kα (4JPS)*

As shown in the **Fig. 6.** L1 was stabilised by two conventional hydrogen bonds with ASN465 and GLN487, a π-donor interaction with ASN465, and hydrophobic contacts with PRO3, PRO447, and Lys678. The limited aromatic and electrostatic reinforcement observed for L1, in comparison to L2 and L3 is likely responsible for its lower binding score. L2 exhibited two conventional hydrogen bonds with GLU710, a π-π T-shaped interaction with His676, and π-alkyl contacts with ARG4 and PRO3. This combination of polar anchoring confers improved complementarity relative to L1. L3 demonstrated the highest predicted affinity, with stabilisation arising from a conventional hydrogen bond and a carbon-hydrogen bond with ARG818, a dual π-cation/electrostatic and hydrogen bond-associated interaction with LYS271, additional π-cation contacts with ARG818, a π-π stacking interaction with PHE666, and π-alkyl with LYS271. The predominance of cation-π and aromatic interactions suggest that the scaffold of L3 is particularly compatible with the charged and hydrophobic residue present in the binding pocket, which accounts for its superior docking score among three ligands.

Bcl-2 interactions

For Bcl-2, the affinity trend changed to L1(-8.9 kcal/mol) > L2(-8.6 kcal/mol) > L3(-8.1 kcal/mol), making L1 the best-performing ligand for the target. The LE and K_d follow the same trend.

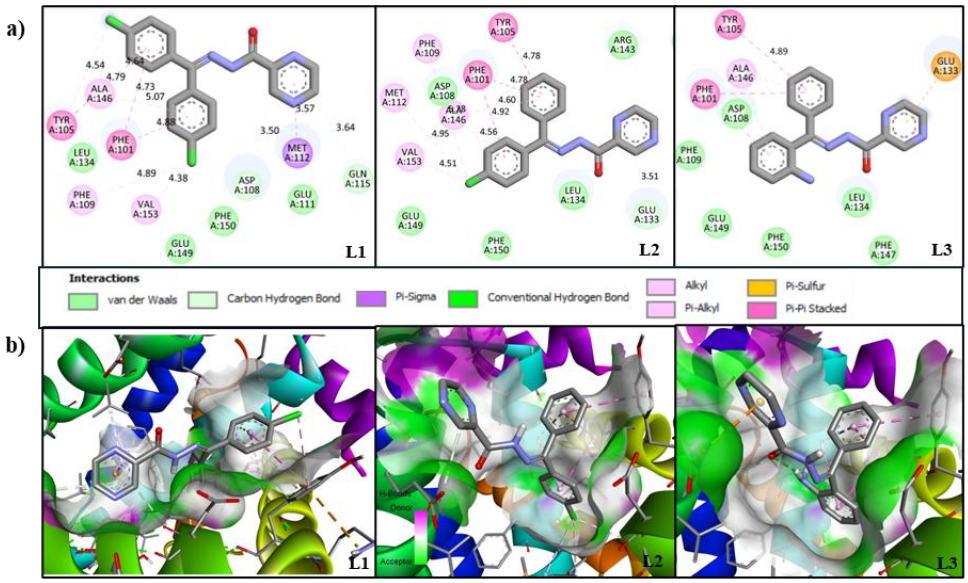

Fig. 7. a) 2D and b) 3D docking images of ligands L1-L3 with *Bcl-2 (4LXD)*

L1 was stabilised through two carbon-hydrogen bonds with ASP108 and GLN115, a π-sigma and a π-sulfur interaction with MET112, three aromatic contacts with PHE101 and TYR105, an alkyl interaction with VAL153, and additional π-alkyl contacts with TYR105, PHE109, and ALA146. This extensive hydrophobic and aromatic interaction network, together with polar contacts, indicates a high degree of shape complementarity, which accounts for the superior docking score of L1 among the tested ligands. L2 also exhibited favourable binding, with stabilisation arising from a carbon-hydrogen bond with GLU133, aromatic contacts with PHE101 and TYR105, alkyl interactions with MET112 and VAL153, and π-alkyl contacts with PHE109 and ALA146. The reduced number of polar and sulfur-associated interactions for L2, compared to L1, likely results in its marginally lower stabilisation energy. L3 displayed the poor binding score, with stabilisation primarily due to a single π-anion interaction with GLU133, aromatic contacts with PHE101 and TYR105, and π-alkyl contacts with ALA146. The absence of conventional hydrogen bonding and the relatively simple interaction profile suggest a less deeply anchored binding mode, consistent with its lower predicted affinity. Which is depicted in **Fig. 7.**

IV. Conclusions

The present research illustrates the synthesis, structural characterization, and biological evaluation of three pyrazine-2-carbohydrazide Schiff base ligands (L1–L3) and their corresponding ruthenium(II) complexes (RuL1–RuL3). Spectroscopic techniques (FT-IR, NMR, UV-Vis, HRMS) and single-crystal X-ray diffraction(L1 and L3) confirmed a neutral N, N-bidentate coordination mode through the pyrazine and azomethine nitrogen atoms, while the amide carbonyl group was not involved in metal coordination. Evaluation of cytotoxicity against Colorectal Carcinoma (Caco-2) cells revealed an electronic trend among the free ligands (L3 > L2 > L1), which can be attributed to the electron-donating and hydrogen-bonding properties of the 2-aminophenyl substituent present in L3. Coordination with ruthenium(II) resulted in enhanced antiproliferative activity, particularly at 24

hours, with RuL2 and RuL3 demonstrating sustained cytotoxic effects at 48 hours. These results indicate that ruthenium(II) coordination may facilitate increased cytotoxicity by promoting cellular uptake and improving the stability of the complexes. The observed cytotoxicity trends were found to be in agreement with the molecular docking results. The ligand L1 exhibited the highest predicted binding affinity toward Bcl-2 (4LXD) (−8.9 kcal/mol), which was attributed to an extensive network of hydrophobic and aromatic interactions. In contrast, the binding affinities of the ligands toward EGFR (1M17) and PI3Kα (4JPS) were greater for L3, which was capable of forming dual hydrogen bonds and multiple cation-π interactions at both targets. The consistent ranking of L3 as the most potent ligand in kinase-target affinity, as well as its lowest cellular IC_{50} value among the free ligands, suggests that engagement with EGFR and PI3Kα may contribute significantly to the observed cytotoxicity, rather than binding affinity alone being the determining factor. The enhanced hydrogen-bonding and electrostatic interactions identified for L3 in computational studies are consistent with its increased cellular activity, providing a structural basis that connects the in silico and in vitro findings. These correlations indicate that RuL2 and RuL3 represent promising candidates for further mechanistic, *in-vivo*, and pharmacokinetic studies.

Acknowledgements

The author acknowledges the KSTePS DST, Govt of Karnataka, for providing financial support; the University Scientific Instrument Centre (USIC and SAIF DST, Karnatak University, Dharwad; and SIC, Central University of Karnataka, for the characterisation facility.

Authors contributions

CRediT: **Shivaraj S Dolli:** conceptualisation, investigation, writing original draft; **Laxmi A Jagatap:** Formal analysis; **Ramesh Vadavi:** Methodology**;** Tathagata Chakraborthy: Data curation; **Oruganti Anjaneyulu:** Validation; **Kalagouda Gudasi:** Supervision, Writing - review & editing.

Disclosure of interest

The authors report there are no competing interests to declare.

References

[1] F. Bray, M. Laversanne, H. Sung, J. Ferlay, R.L. Siegel, I. Soerjomataram, A. Jemal, Global cancer statistics 2022: GLOBOCAN estimates of incidence and mortality worldwide for 36 cancers in 185 countries, CA Cancer J. Clin. 74 (2024) 229–263. https://doi.org/10.3322/caac.21834.

[2] S. Dasari, P. Bernard Tchounwou, Cisplatin in cancer therapy: Molecular mechanisms of action, Eur. J. Pharmacol. 740 (2014) 364–378. https://doi.org/10.1016/j.ejphar.2014.07.025.

[3] L. Amable, Cisplatin resistance and opportunities for precision medicine, Pharmacol. Res. 106 (2016) 27–36. https://doi.org/10.1016/j.phrs.2016.01.001.

[4] G. V. Girichev, N.I. Giricheva, Special Issue "Metal–Organic Coordination Compounds: Synthesis, Structure, Spectra, Applications," Int. J. Mol. Sci. 27 (2026). https://doi.org/10.3390/ijms27062824.

[5] M. Aslam, A.P.S. Raman, I. Rana, M.B. Singh, K.R. Ranjan, C. Verma, A. AlFantazi, P. Singh, K. Kumari, Coordination and organometallic compounds of graphyne and graphdiyne: Synthesis, properties and applications, Coord. Chem. Rev. 543 (2025). https://doi.org/10.1016/j.ccr.2025.216890.

[6] S. Talari, S.M. Ibrahim, B. .P, Ch.L. Prasanna, R. Thomas, G.S. Rao, Advancements in Coordination Chemistry: Design and Applications of Metal Complexes, Oriental Journal Of Chemistry 41 (2025) 708–716. https://doi.org/10.13005/ojc/410302.

[7] S.Y. Lee, C.Y. Kim, T.G. Nam, Ruthenium complexes as anticancer agents: A brief history and perspectives, Drug Des. Devel. Ther. 14 (2020) 5375–5392. https://doi.org/10.2147/DDDT.S275007.

[8] W.M. Motswainyana, P.A. Ajibade, Anticancer Activities of Mononuclear Ruthenium(II) Coordination Complexes, Advances in Chemistry 2015 (2015) 1–21. https://doi.org/10.1155/2015/859730.

[9] P. Miniyar, S. Makhija, Synthesis and characterization of pyrazine-2-carbohydrazide derivatives as antimicrobial agents, Journal of Young Pharmacists 1 (2009) 165. https://doi.org/10.4103/0975-1483.55750.

[10] A. Alsfouk, Pyrazine-based small molecule kinase inhibitors: clinical applications and patent review (2019–2023), Future Med. Chem. 16 (2024) 1899–1921. https://doi.org/10.1080/17568919.2024.2385293.

[11] U.S. Food and Drug Administration. FDA approves gilteritinib for relapsed or refractory acute myeloid leukemia (AML) with a FLT3 mutation. FDA.gov, November 28, 2018., U.S. Food and Drug Administration (2018).

[12] A.E. Eskazan, D. Keskin, Radotinib and its clinical potential in chronic-phase chronic myeloid leukemia patients: an update, Ther. Adv. Hematol. 8 (2017) 237–243. https://doi.org/10.1177/2040620717719851.

[13] A. Ghelli, L. Di Rorà, I. Iacobucci, E. Imbrogno, C. Papayannidis, E. Derenzini, A. Ferrari, V. Guadagnuolo, V. Robustelli, S. Parisi, C. Sartor, M. Chiara Abbenante, S. Paolini, G. Martinelli, Prexasertib, a Chk1/Chk2 inhibitor, increases the effectiveness of conventional therapy in B-/T-cell progenitor acute lymphoblastic leukemia, n.d. www.impactjournals.com/oncotarget/.

[14] L. Cao, S. Chen, R. Sun, C.R. Ashby, L. Wei, Z. Huang, Z.-S. Chen, Darovasertib, a novel treatment for metastatic uveal melanoma, Front. Pharmacol. 14 (2023). https://doi.org/10.3389/fphar.2023.1232787.

[15] B.M. DINNIMATH, P. GOWDA, A. NAIK, DEVELOPMENT OF ORGANOMETALLIC COMPOUNDS OF SCHIFF BASES WITH DIVERSE APPLICATIONS, Int. J. Pharm. Pharm. Sci. (2023) 1–15. https://doi.org/10.22159/ijpps.2023v15i6.47362.

[16] E.G. Mahmoud, E.H. Ismail, A.A. Abdel Aziz, S.A. Abdel-Latif, S.N. Mobarez, Synthesis, spectroscopic, characterization, antimicrobial, DNA interaction, DFT and molecular docking studies of a new Cu(II)-Schiff base complex, Sci. Rep. 16 (2026). https://doi.org/10.1038/s41598-026-44842-5.

[17] Suchita Bondre, Deepika Gupta, Biological Evaluation of Novel Schiff Base Metal Complexes: A Review, International Journal of Scientific Research and Technology (2026).

[18] S.Y. Lee, C.Y. Kim, T.G. Nam, Ruthenium complexes as anticancer agents: A brief history and perspectives, Drug Des. Devel. Ther. 14 (2020) 5375–5392. https://doi.org/10.2147/DDDT.S275007.
[19] L.G. Julius, M.O. Koobotse, T.B. Demissie, J.T.P. Matshwele, F.M. Nareetsile, T. Molefe, K. Bati, D.O. Nkwe, D.T. Mapolelo, Synthesis, characterization, anticancer and antibacterial studies of ruthenium(II/III) benzimidazole complexes, Results Chem. 17 (2025). https://doi.org/10.1016/j.rechem.2025.102647.
[20] R. Zein, I. Alghoraibi, C. Soukkarieh, A. Salman, A. Alahmad, In-vitro anticancer activity against Caco-2 cell line of colloidal nano silver synthesized using aqueous extract of Eucalyptus Camaldulensis leaves, Heliyon 6 (2020). https://doi.org/10.1016/j.heliyon.2020.e04594.
[21] S. Wu, Y. Zhang, Z. Lin, M. Wei, Global burden of colorectal cancer in 2022 and projections to 2050: incidence and mortality estimates from GLOBOCAN, BMC Cancer 25 (2025). https://doi.org/10.1186/s12885-025-15138-0.
[22] J. Ji, X. Chen, C.J. Wang, A.Q. Jia, Q.F. Zhang, Syntheses, structures and electrochemical properties of ruthenium(II/III) complexes with tetradentate Schiff base ligands, J. Coord. Chem. 72 (2019) 480–490. https://doi.org/10.1080/00958972.2019.1566541.
[23] G.M. Sheldrick, SHELXT - Integrated space-group and crystal-structure determination, Acta Crystallogr. A 71 (2015) 3–8. https://doi.org/10.1107/S2053273314026370.
[24] O. V. Dolomanov, L.J. Bourhis, R.J. Gildea, J.A.K. Howard, H. Puschmann, *OLEX2* : a complete structure solution, refinement and analysis program, J. Appl. Crystallogr. 42 (2009) 339–341. https://doi.org/10.1107/S0021889808042726.
[25] Green synthesis of chromium oxide nanoparticles using Simarouba glauca leaf extract and its biomedical applications, (n.d.).
[26] G.M. Morris, R. Huey, W. Lindstrom, M.F. Sanner, R.K. Belew, D.S. Goodsell, A.J. Olson, AutoDock4 and AutoDockTools4: Automated docking with selective receptor flexibility, J. Comput. Chem. 30 (2009) 2785–2791. https://doi.org/10.1002/jcc.21256.
[27] B. Susmita Rayawgol, K. Sujatha, N.P. Dalbanjan, S.K. Praveen Kumar, S.K. Rajappa, Development of novel, green, efficient approach for the synthesis of indazole and its derivatives; insights into their pharmacological and molecular docking studies, Journal of the Indian Chemical Society 101 (2024) 101178. https://doi.org/10.1016/j.jics.2024.101178.
[28] O. Trott, A.J. Olson, AutoDock Vina: Improving the speed and accuracy of docking with a new scoring function, efficient optimization, and multithreading, J. Comput. Chem. 31 (2010) 455–461. https://doi.org/10.1002/jcc.21334.
[29] B. Kaya, H. Tahtacı, B. Çiftçi, H.E. Duran, A. Necip, M. Işık, Ş. Beydemir, Discovery of Hydrazine Clubbed Thiazoles as Potential Antidiabetic Agents: Synthesis, Biological Evaluation, and Molecular Docking Studies, Drug Dev. Res. 86 (2025). https://doi.org/10.1002/ddr.70060.
[30] N.P. Dalbanjan, A.A. Nadaf, A.J. Kadapure, S.R. Naik, S.M. Kakambi, P.K. Naduvinamani, D. Kencharaddi, A. Nadaf, B. Devkar, M. Yaseen, S.K. Praveen Kumar, In-vitro and in-silico evaluation of antihyperglycemic, antioxidant, anti-inflammatory activities of selected (2Z)-2-((E)(2′hydroxy)-4(benzylideneamino)phenyl)-3-(1-methyl-1H-imidazole-2-yl)acrylonitrile derivatives, Journal of the Indian Chemical Society 102 (2025) 101592. https://doi.org/10.1016/j.jics.2025.101592.
[31] G. Moya-Alvarado, O. Yañez, N. Morales, A. González-González, C. Areche, M.T. Núñez, A. Fierro, O. García-Beltrán, Coumarin-Chalcone Hybrids as Inhibitors of MAO-B: Biological Activity and In Silico Studies, Molecules 26 (2021) 2430. https://doi.org/10.3390/molecules26092430.
[32] N. Chethanakumar, M.B. Budri, K.B. Gudasi, R.S. Vadavi, M.K. Patil, V.M. Kumbar, S.R. Inamdar, Tri-armed Schiff base fluorescent sensor for the rapid recognition of Zn(ii): application in live cell imaging, test strips and TLC, Analytical Methods 16 (2024) 4743–4754. https://doi.org/10.1039/d4ay00774c.
[33] N. Chethanakumar, M.B. Budri, K.B. Gudasi, R.S. Vadavi, M.K. Patil, V.M. Kumbar, S.R. Inamdar, A pyrene-induced PET-based chemosensor for biologically important Zn(ii) ions: application in test strips and live cell imaging studies, Analytical Methods 16 (2024) 1934–1947. https://doi.org/10.1039/d4ay00252k.

Supplementary data

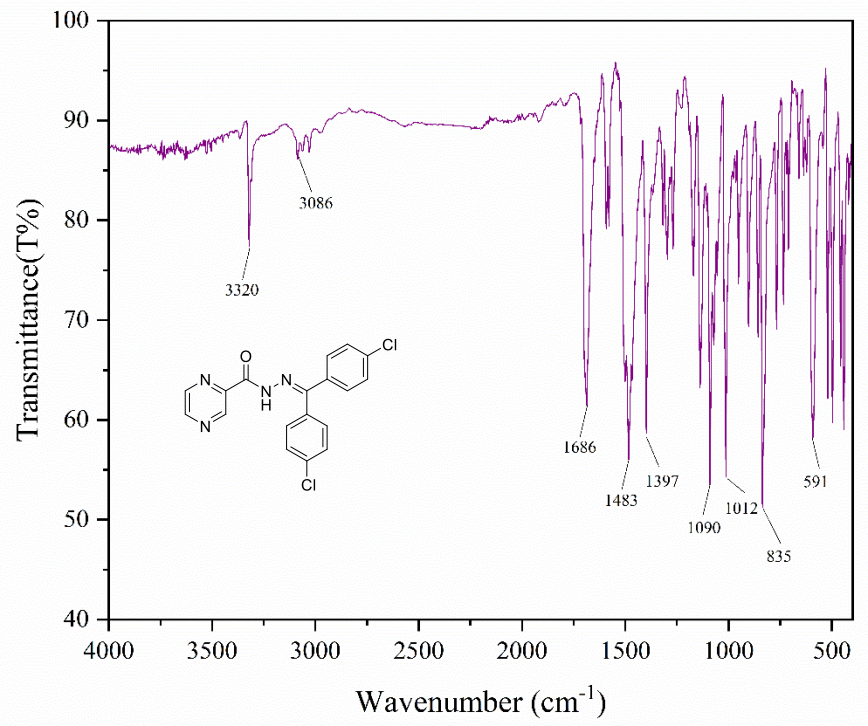

Fig S1. FT-IR of ligand L1

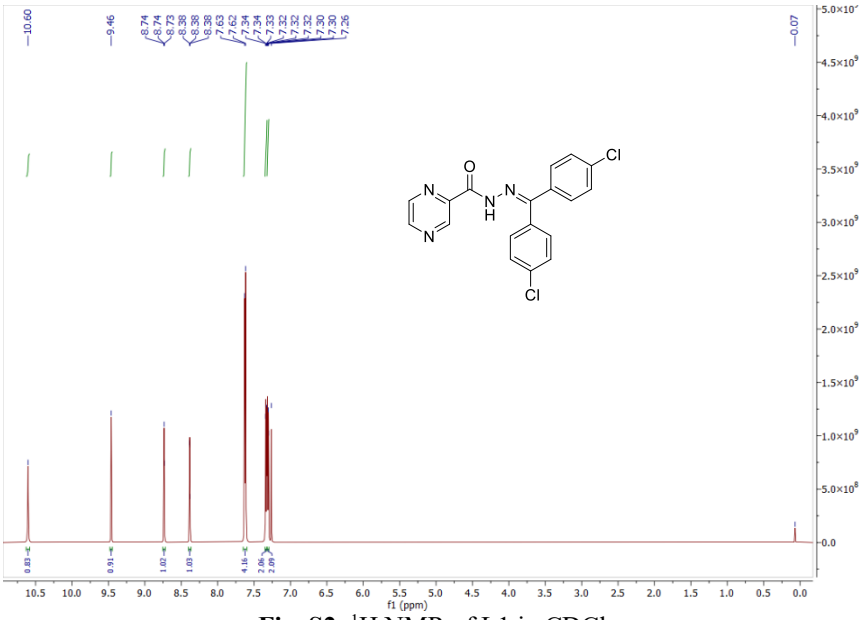

Fig. S2. ^{1}H NMR of L1 in $CDCl_3$

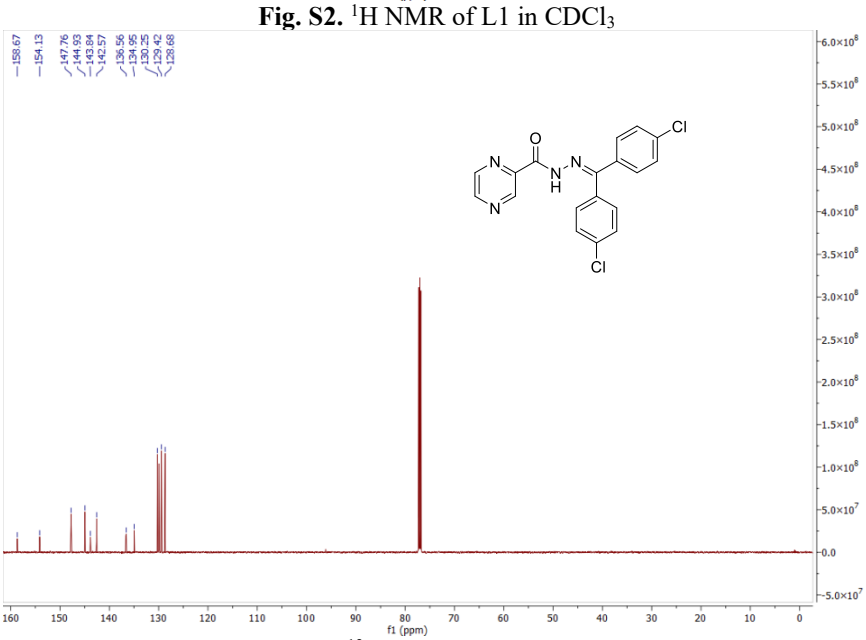

Fig. S3. ^{13}C NMR of L1 in $CDCl_3$

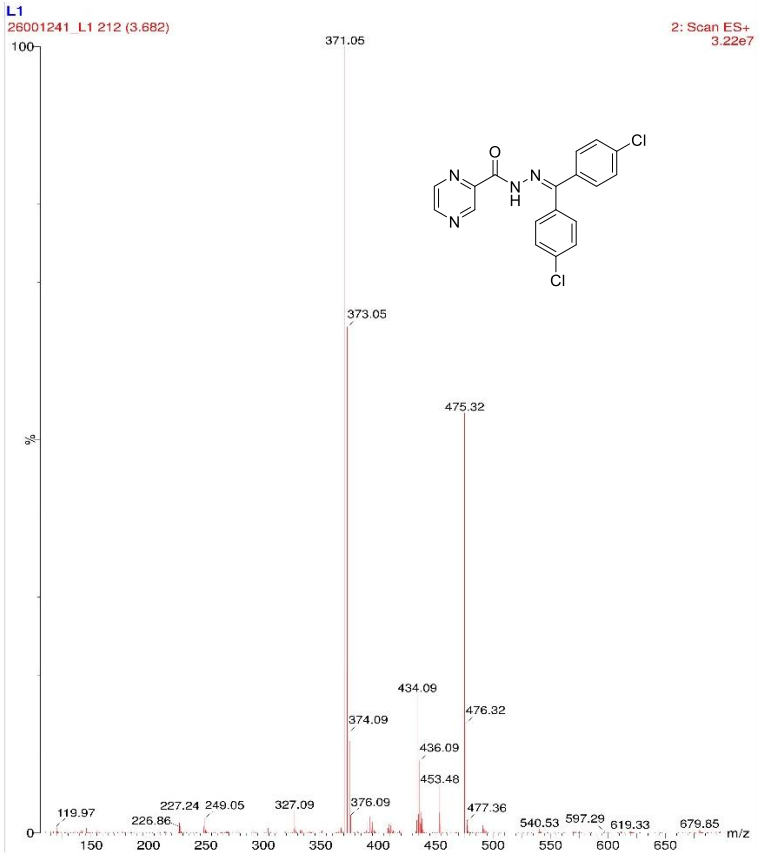

Fig. S4. LCMS spectrum of L1 $[M]^+$ m/z 371.05

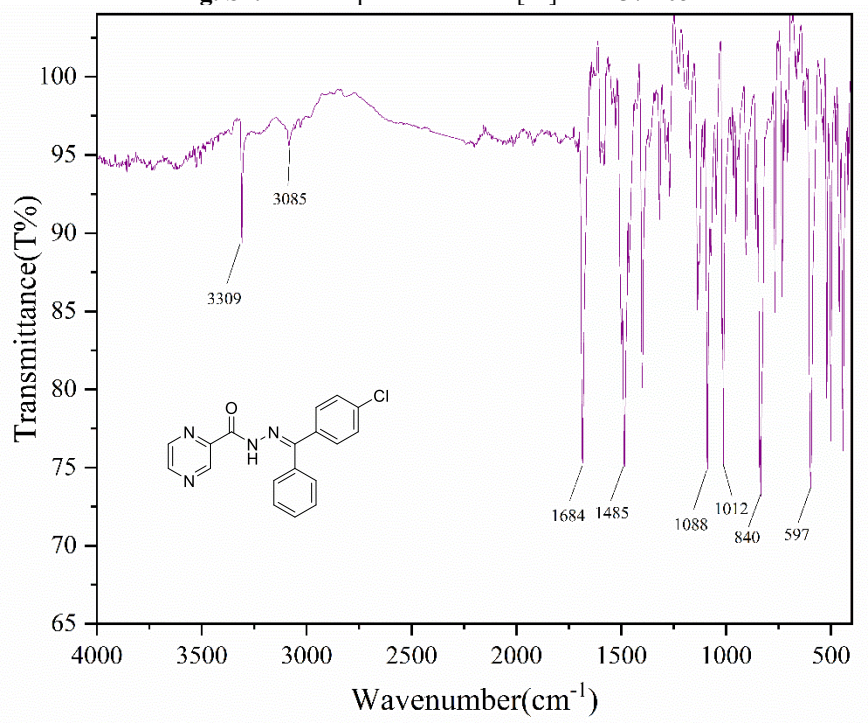

Fig S5. FT-IR of ligand L2

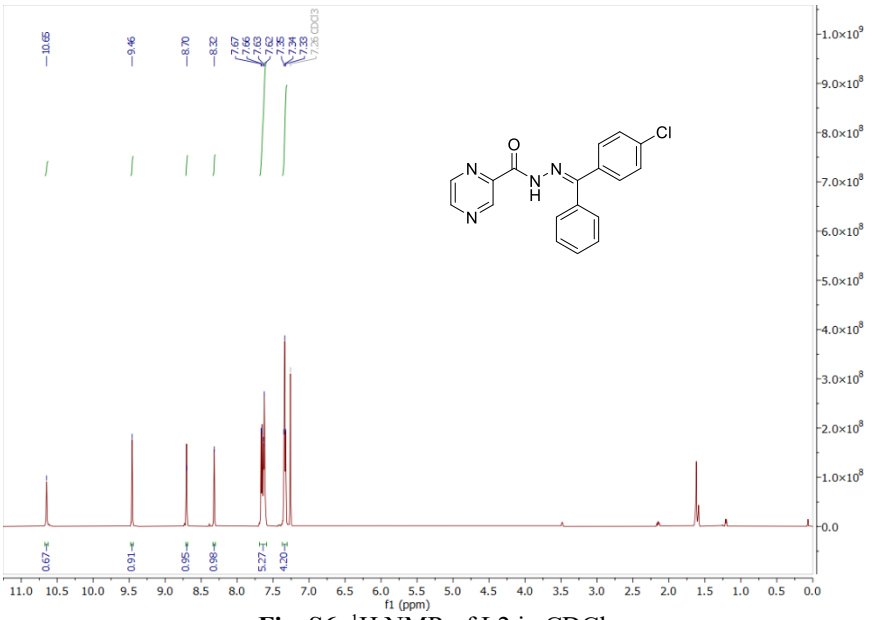

Fig. S6. ^{1}H NMR of L2 in $CDCl_3$

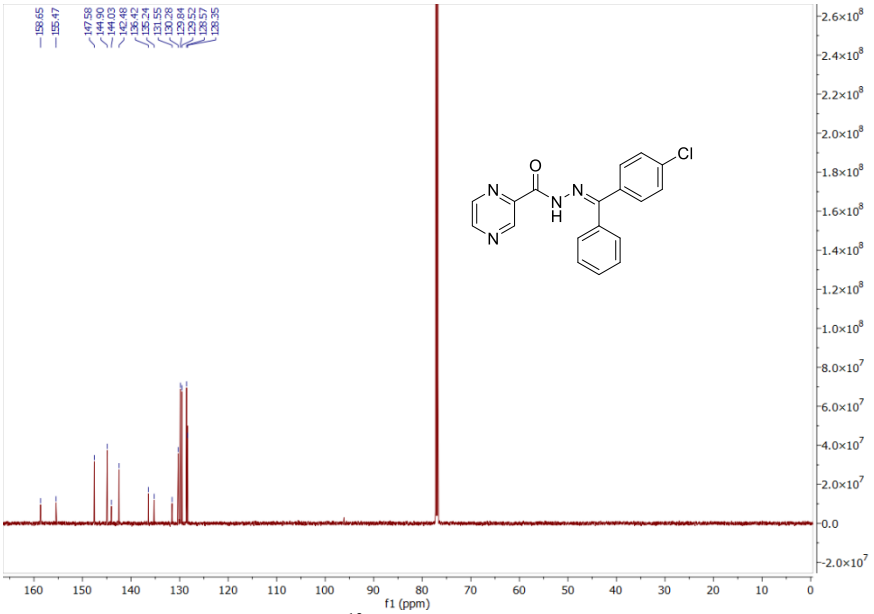

Fig. S7. ^{13}C NMR of L2 in $CDCl_3$

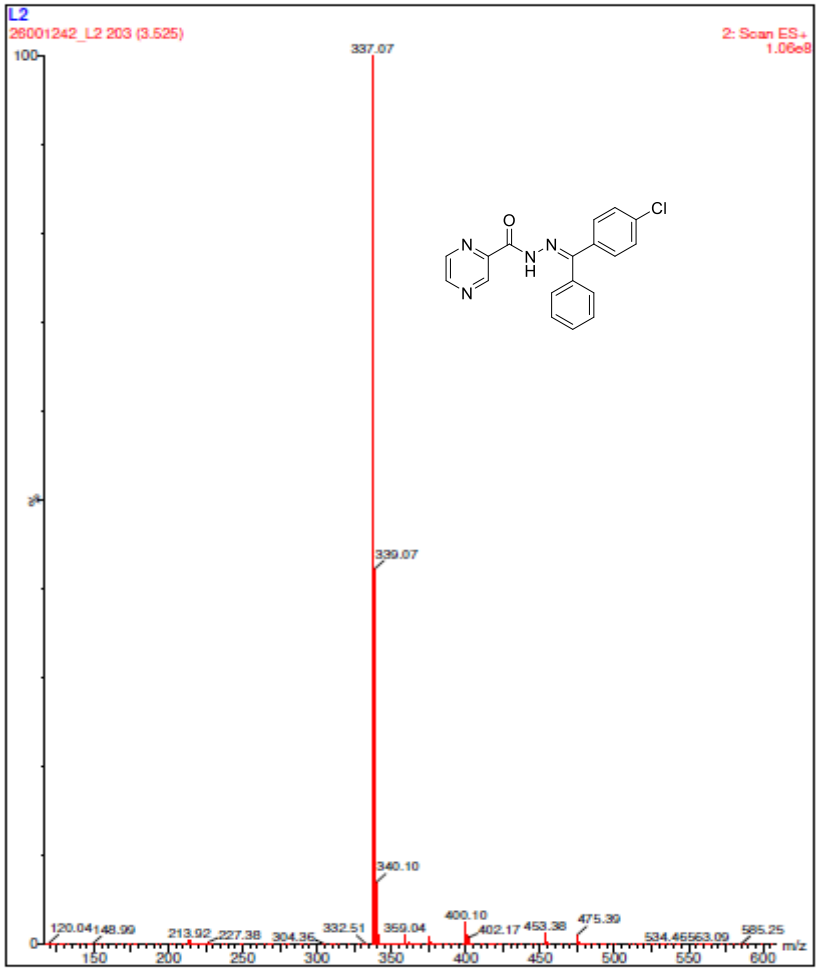

Fig. S8. LC-MS spectrum of L2 $[M+H]^+$ m/z 337.07

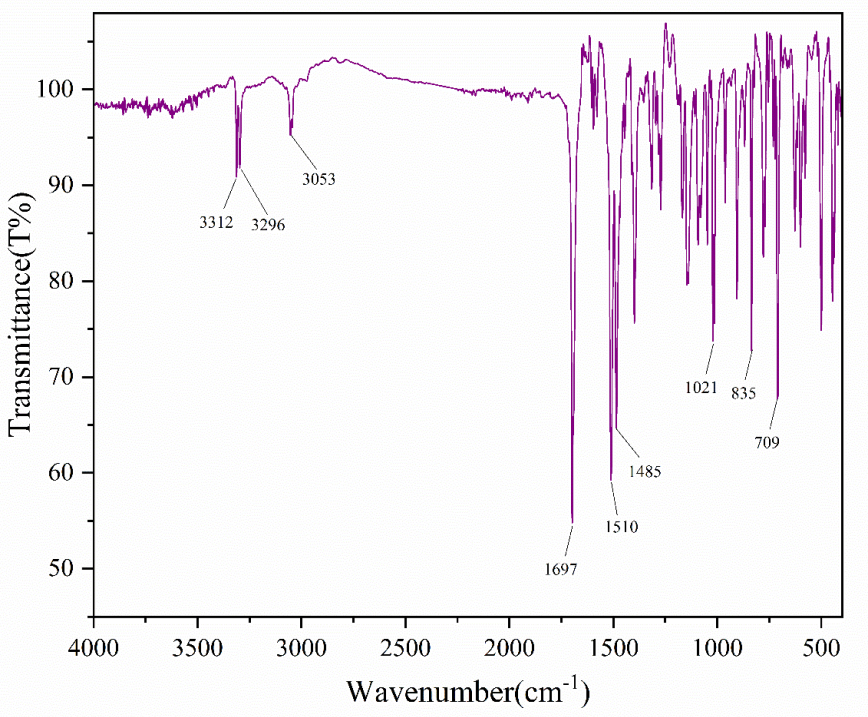

Fig S9. FT-IR of ligand L3

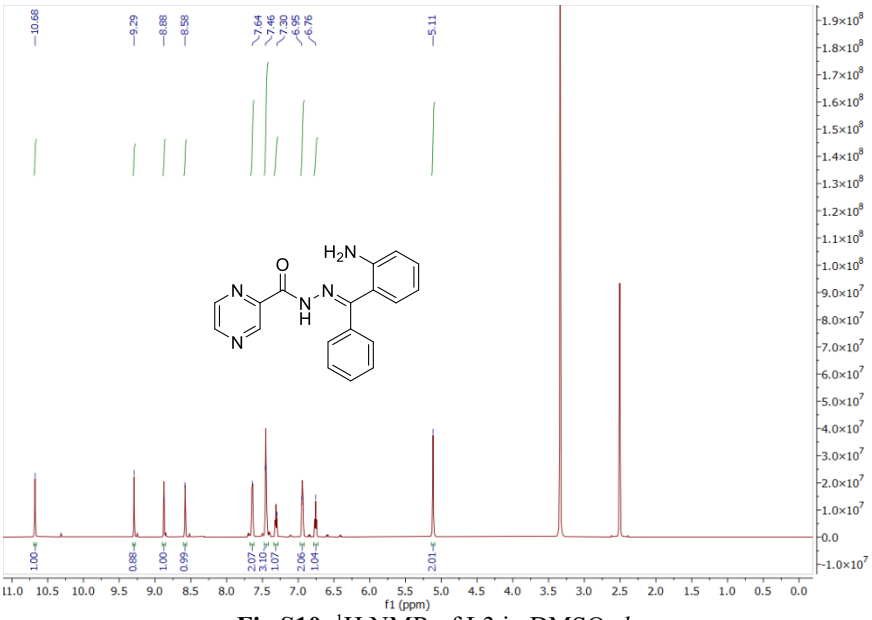

Fig S10. ^{1}H NMR of L3 in DMSO-d_6

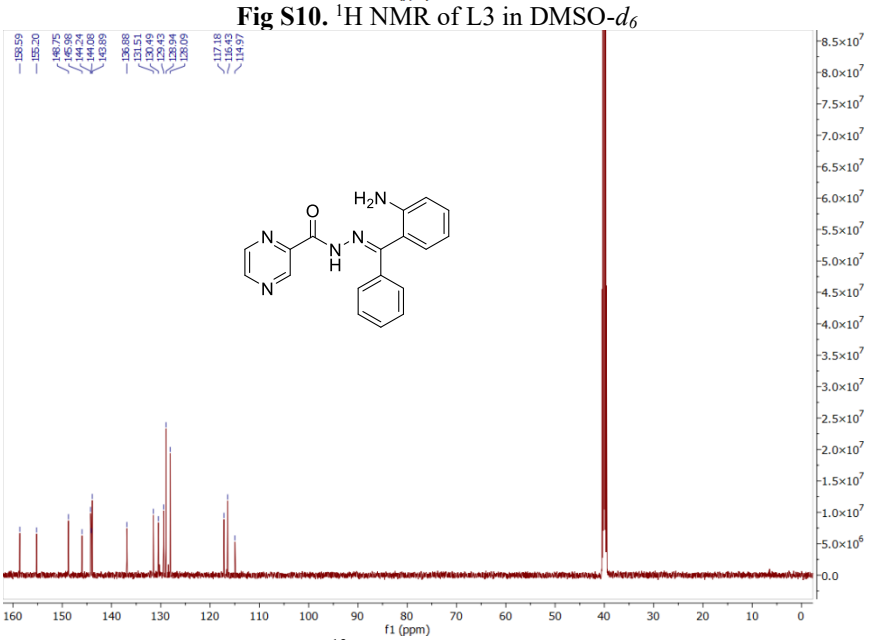

Fig S11. ^{13}C NMR of L3 in DMSO-d_6

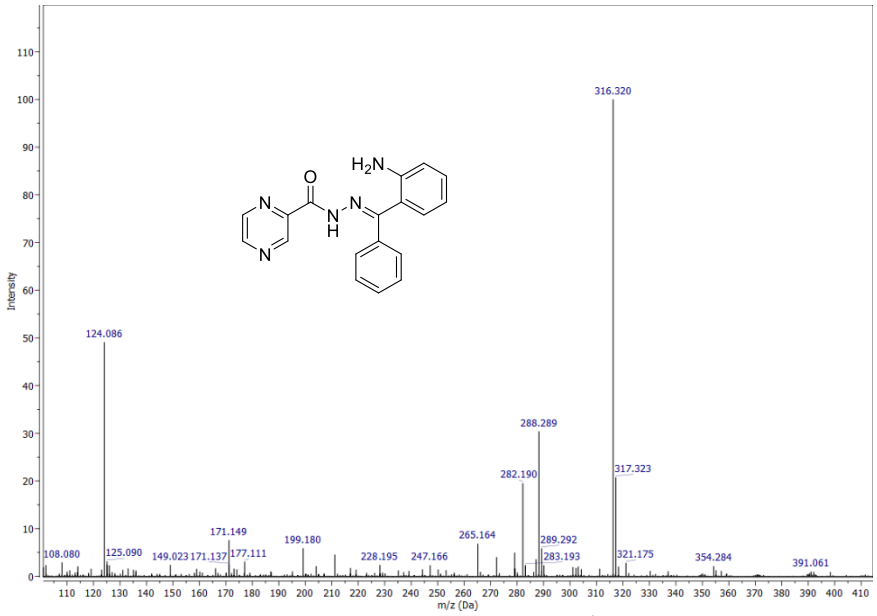

Fig. S12. HRMS spectrum of L3 $[M-H]^+$ m/z 316.32

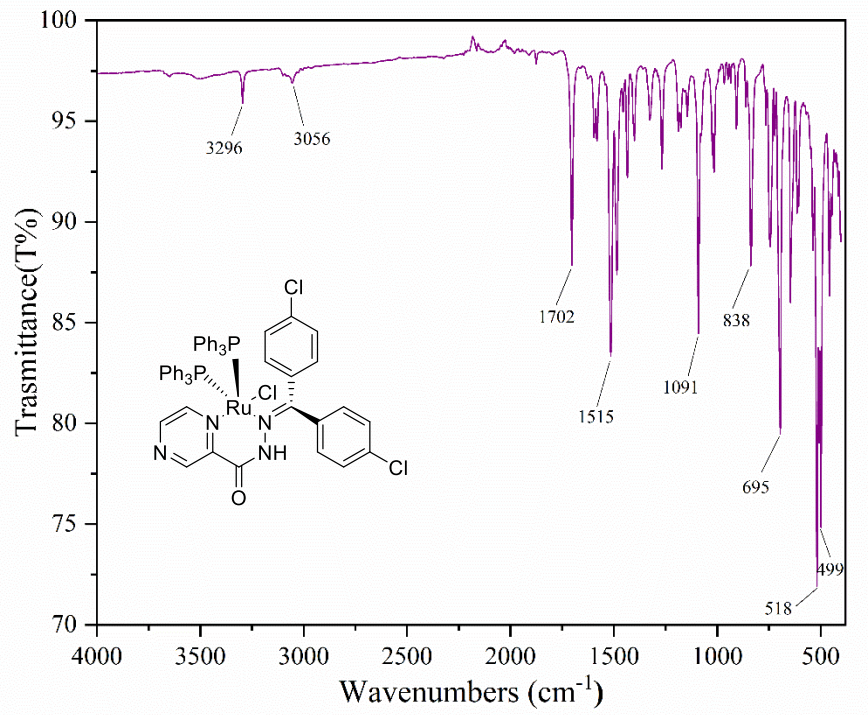

Fig S13. FT-IR of RuL1

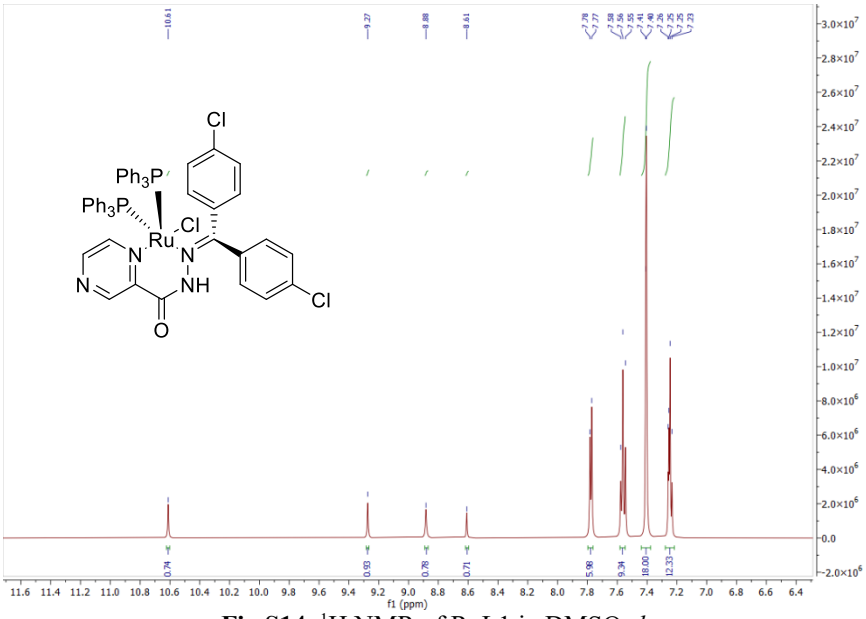

Fig S14. ^{1}H NMR of RuL1 in DMSO-d_6

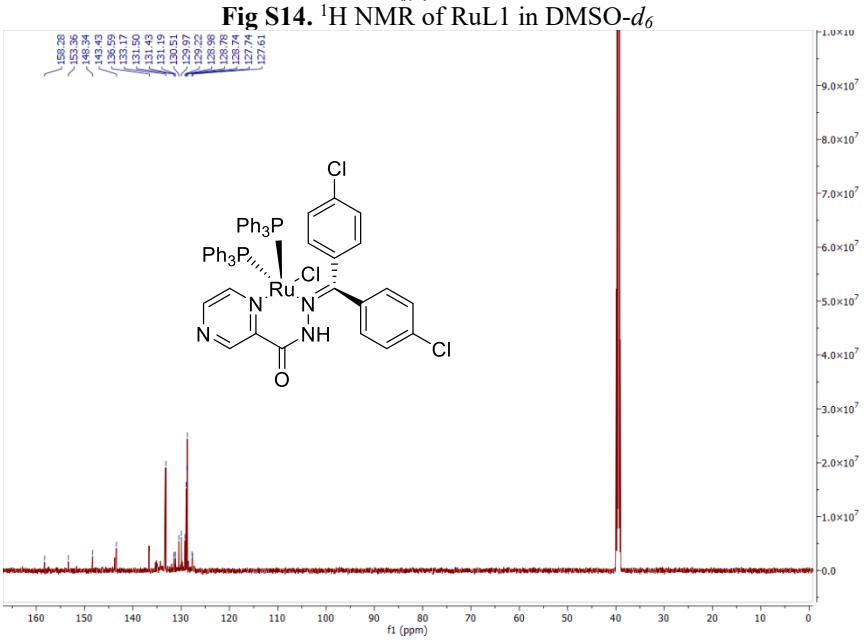

Fig S15. ^{13}C NMR of RuL1 in DMSO-d_6

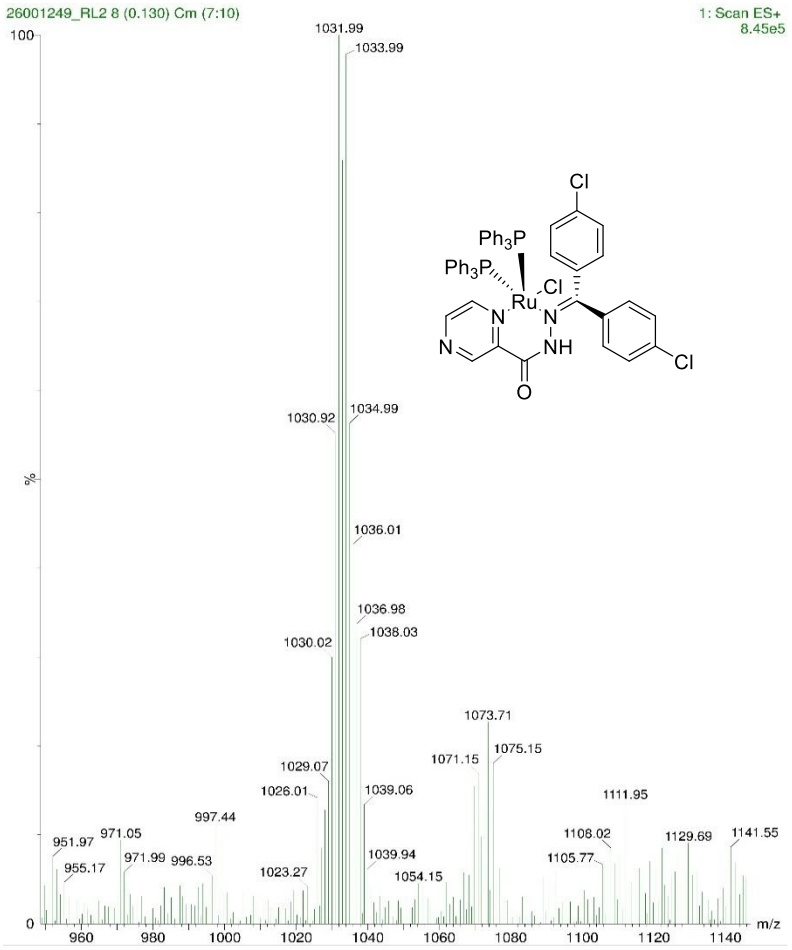

Fig. S16. LC-MS spectrum of RuL1 $[M+H]^+$ m/z 1031

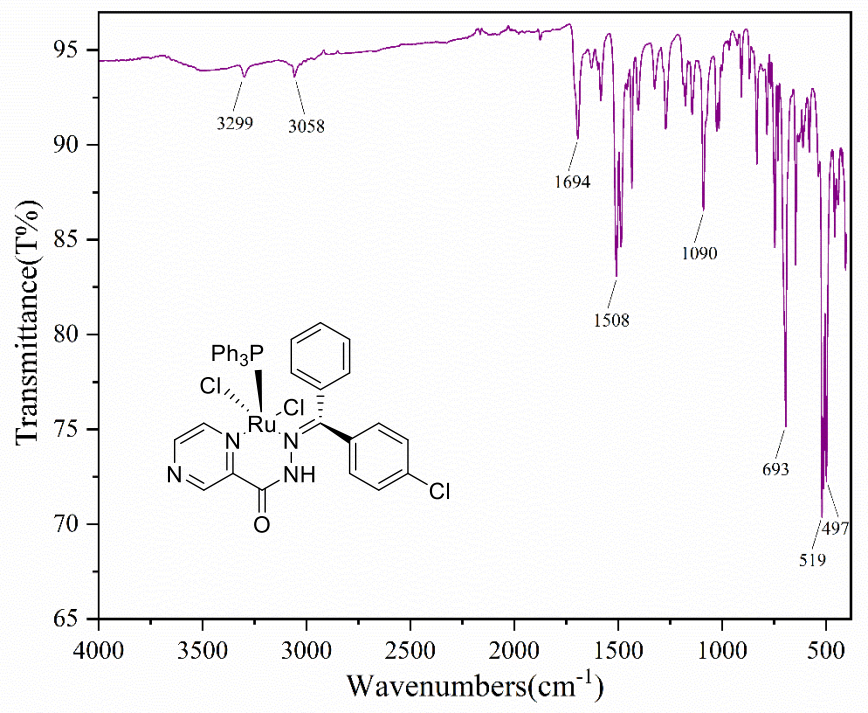

Fig S17. FT-IR of RuL2

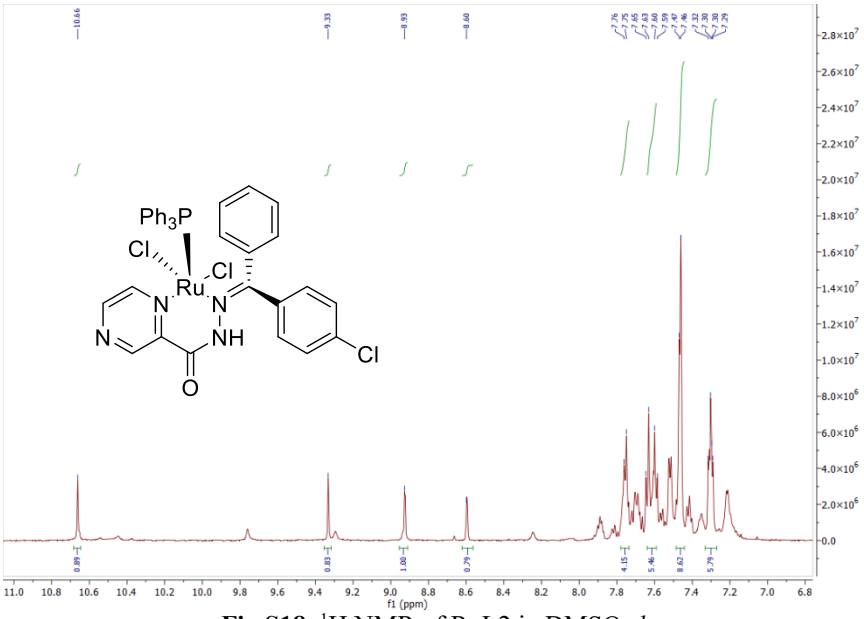

Fig S18. ^{1}H NMR of RuL2 in DMSO-d_6

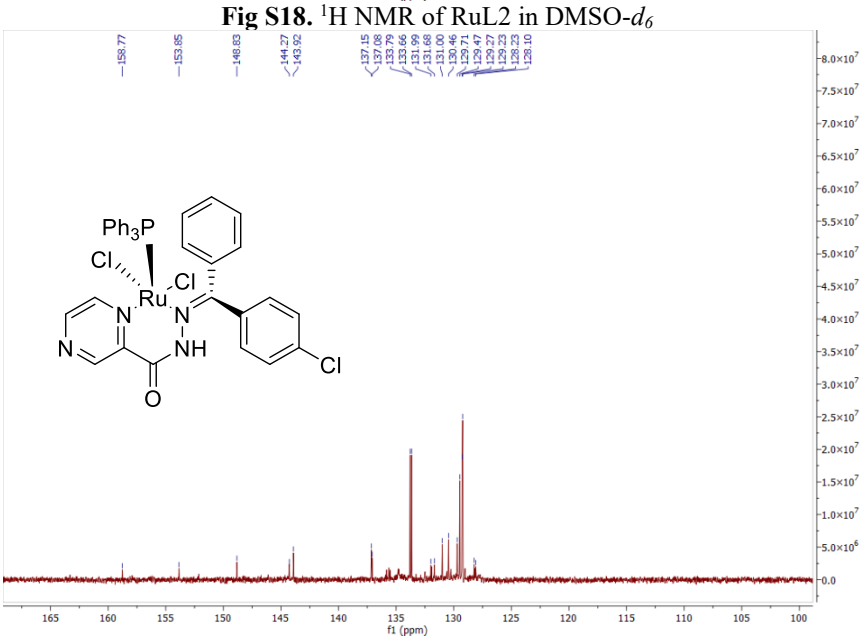

Fig S19. ^{13}C NMR of RuL2 in DMSO-d_6

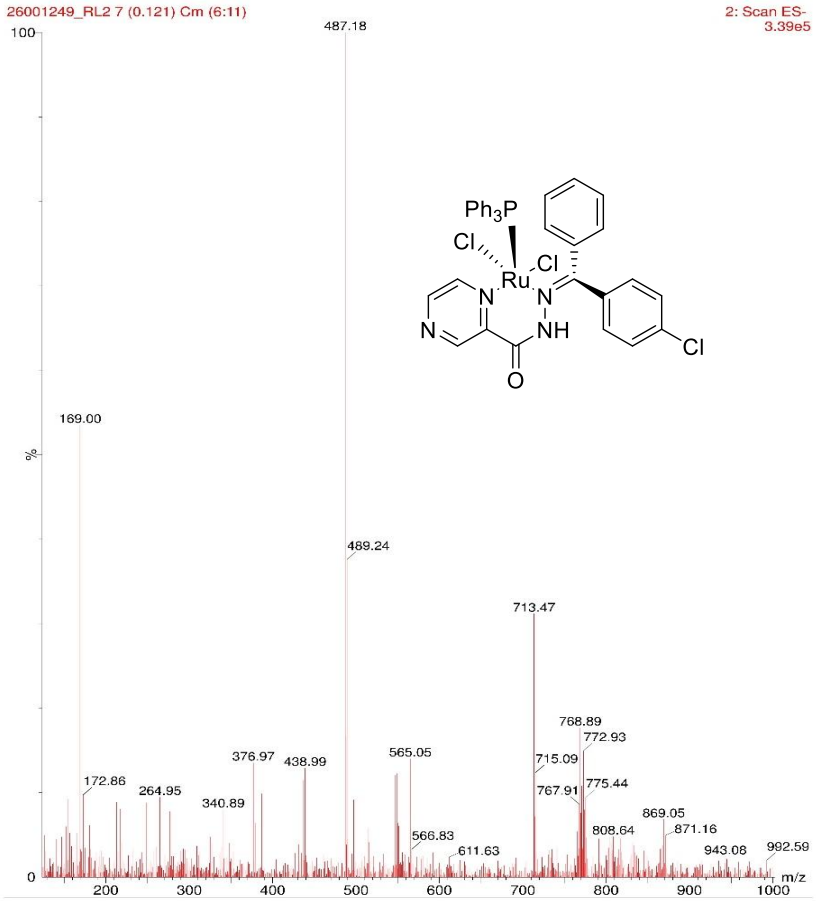

Fig. S20. LC-MS spectrum of RuL2 $[M\text{-}PPh_3]^+$ m/z 487

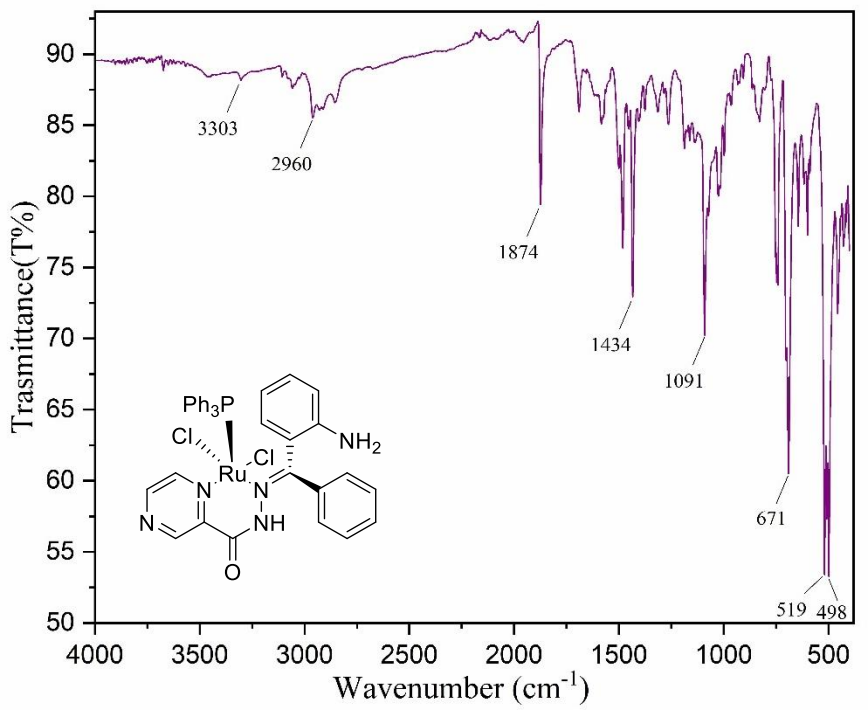

Fig S21. FT-IR of RuL3

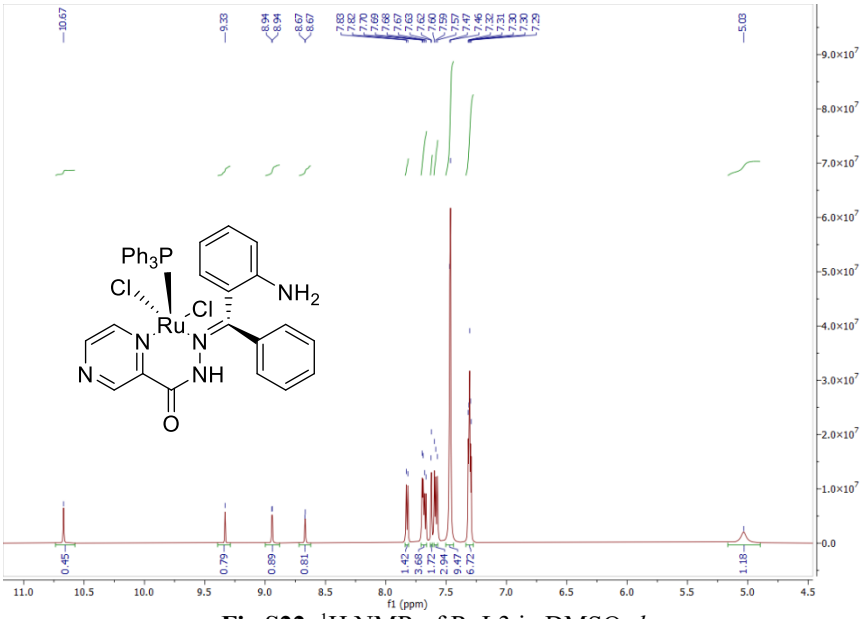

Fig S22. ^{1}H NMR of RuL3 in DMSO-d_6

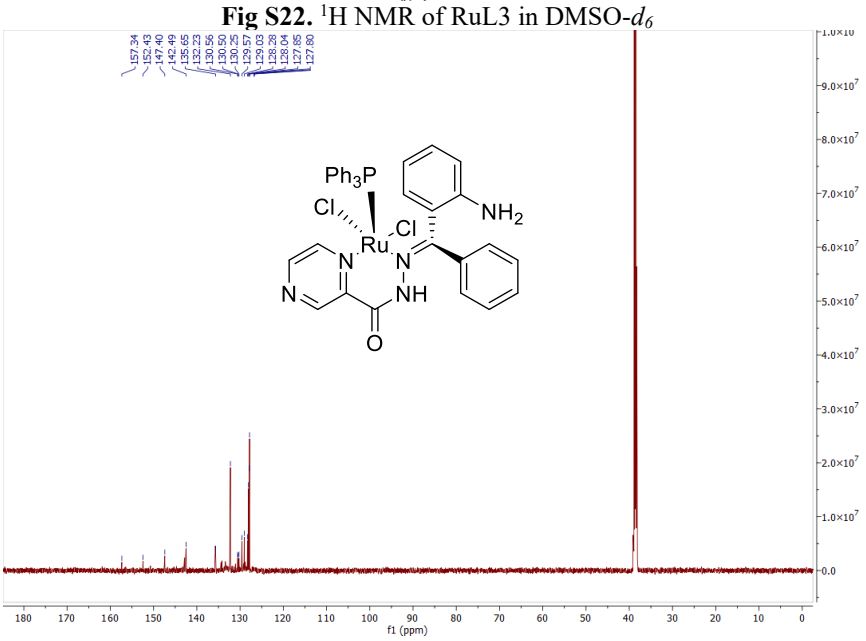

Fig S23. ^{13}C NMR of RuL3 in DMSO-d_6

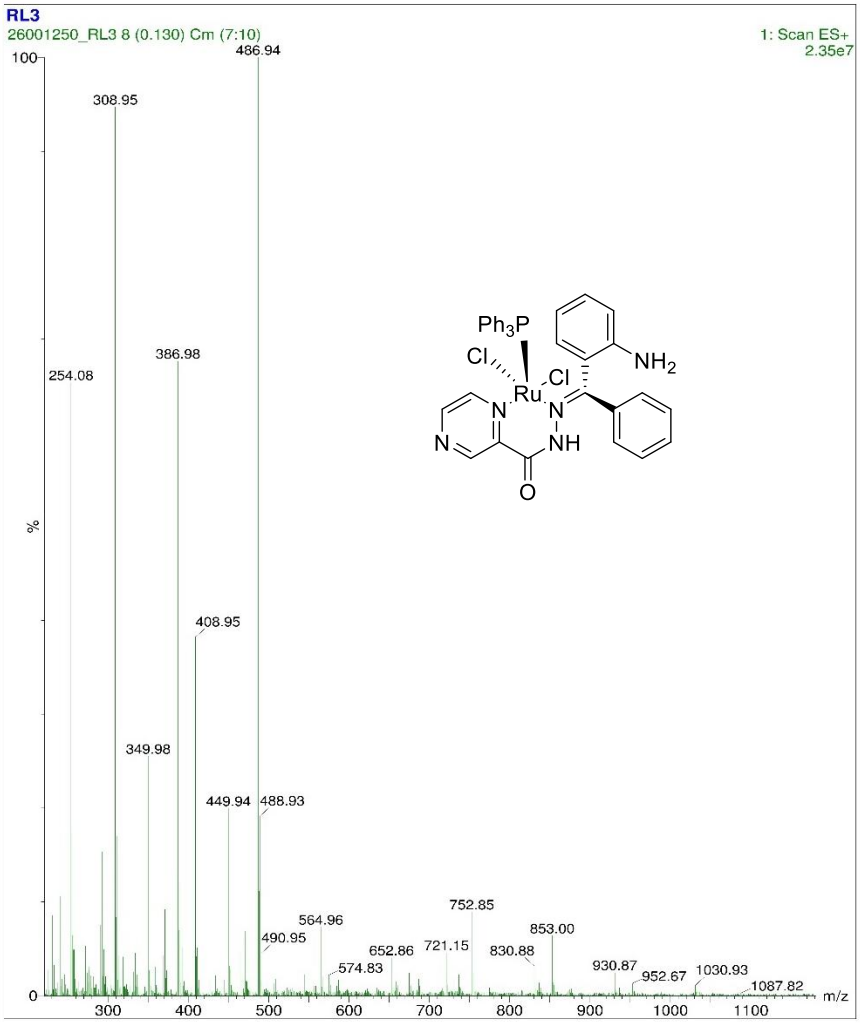

Fig. S24. LC-MS spectrum of RuL3 $[M\text{-}2H\text{-}PPh_3]^+$ m/z 486.94

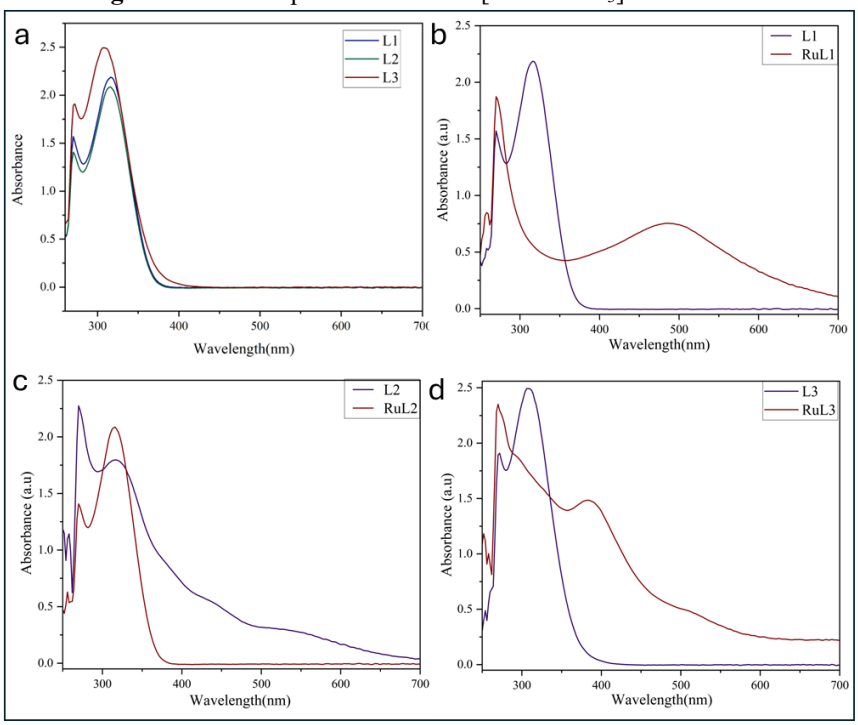

Fig S25. UV-Vis. Sprctra of **a)** Ligands L1-L3 **b)** L1 and RuL1 **c)** L2 and RuL2 **d)** L3 and RuL3 in DMF solvent

Table S1: Bond Lengths in Å for **L1**.

Atom	Atom	Length/Å	Atom	Atom	Length/Å
Cl01	C00I	1.743(2)	C00B	C00D	1.382(3)
Cl02	C00L	1.746(3)	C00B	C00M	1.389(3)
O003	C009	1.218(3)	C00C	C00E	1.388(3)
N004	N005	1.380(2)	C00C	C00H	1.388(3)
N004	C009	1.356(3)	C00D	C00K	1.382(3)
N005	C00A	1.283(3)	C00E	C00F	1.379(3)
N006	C008	1.333(3)	C00F	C00I	1.375(4)
N006	C00J	1.334(3)	C00H	C00O	1.385(4)
N007	C00G	1.335(3)	C00I	C00O	1.369(4)
N007	C00N	1.312(4)	C00J	C00N	1.381(4)
C008	C009	1.490(3)	C00K	C00L	1.375(4)
C008	C00G	1.373(3)	C00L	C00P	1.356(4)
C00A	C00B	1.483(3)	C00M	C00P	1.380(4)
C00A	C00C	1.486(3)			

Table S2: Bond Angles in ° for **L1**.

Atom	Atom	Atom	Angle/°	Atom	Atom	Atom	Angle/°
C009	N004	N005	118.29(18)	C00H	C00C	C00E	118.3(2)
C00A	N005	N004	118.24(19)	C00K	C00D	C00B	120.6(2)
C00J	N006	C008	115.2(2)	C00F	C00E	C00C	121.3(2)
C00N	N007	C00G	115.1(2)	C00I	C00F	C00E	119.0(2)
N006	C008	C009	119.00(18)	N007	C00G	C008	122.8(2)
N006	C008	C00G	121.9(2)	C00C	C00H	C00O	120.8(2)
C00G	C008	C009	119.1(2)	C00F	C00I	Cl01	118.8(2)
O003	C009	N004	124.67(19)	C00F	C00I	C00O	121.4(2)
O003	C009	C008	121.33(19)	C00O	C00I	Cl01	119.75(19)
N004	C009	C008	114.00(18)	N006	C00J	C00N	122.1(2)
N005	C00A	C00B	124.43(19)	C00D	C00K	C00L	118.8(3)
N005	C00A	C00C	116.0(2)	C00K	C00L	Cl02	118.4(2)
C00B	C00A	C00C	119.60(18)	C00P	C00L	Cl02	119.6(2)
C00D	C00B	C00A	120.18(19)	C00P	C00L	C00K	122.0(2)
C00D	C00B	C00M	118.7(2)	C00P	C00M	C00B	120.9(3)
C00M	C00B	C00A	121.1(2)	N007	C00N	C00J	122.8(2)
C00E	C00C	C00A	120.75(19)	C00I	C00O	C00H	119.2(2)
C00H	C00C	C00A	121.0(2)	C00L	C00P	C00M	118.9(2)

Table S3: Bond Lengths in Å for **L3**

Atom	Atom	Length/Å	Atom	Atom	Length/Å
O001	C00B	1.2185(19)	C009	C00F	1.397(2)
N002	N003	1.3801(18)	C00A	C00E	1.390(2)
N002	C00B	1.341(2)	C00A	C00H	1.395(2)
N003	C008	1.2928(19)	C00B	C00C	1.497(2)
N004	C007	1.359(2)	C00C	C00G	1.381(2)
N005	C00C	1.327(2)	C00D	C00J	1.365(3)
N005	C00M	1.330(2)	C00E	C00K	1.383(3)
N006	C00G	1.332(2)	C00F	C00I	1.377(3)
N006	C00L	1.317(3)	C00H	C00N	1.386(3)
C007	C009	1.407(2)	C00I	C00J	1.379(3)
C007	C00D	1.400(2)	C00K	C00O	1.378(3)
C008	C009	1.488(2)	C00L	C00M	1.374(3)
C008	C00A	1.485(2)	C00N	C00O	1.367(3)

Table S4: Bond Angles in ° for **L3**.

Atom	Atom	Atom	Angle/°	Atom	Atom	Atom	Angle/°
C00B	N002	N003	120.02(13)	C00C	C00B	O001	121.72(14)
C008	N003	N002	116.38(12)	C00C	C00B	N002	113.30(13)
C00M	N005	C00C	115.72(16)	C00B	C00C	N005	118.05(14)
C00L	N006	C00G	115.32(16)	C00G	C00C	N005	121.59(15)
C009	C007	N004	121.83(14)	C00G	C00C	C00B	120.35(14)
C00D	C007	N004	120.08(15)	C00J	C00D	C007	121.51(18)
C00D	C007	C009	118.09(15)	C00K	C00E	C00A	120.57(17)
C009	C008	N003	125.12(13)	C00I	C00F	C009	121.29(18)
C00A	C008	N003	115.98(13)	C00C	C00G	N006	122.56(17)
C00A	C008	C009	118.78(13)	C00N	C00H	C00A	120.09(18)

C008	C009	C007	122.88(13)	C00J	C00I	C00F	119.33(18)
C00F	C009	C007	119.16(15)	C00I	C00J	C00D	120.56(17)
C00F	C009	C008	117.96(14)	C00O	C00K	C00E	120.17(19)
C00E	C00A	C008	121.07(14)	C00M	C00L	N006	122.62(17)
C00H	C00A	C008	120.34(14)	C00L	C00M	N005	122.18(18)
C00H	C00A	C00E	118.59(15)	C00O	C00N	C00H	120.68(18)
N002	C00B	O001	124.98(14)	C00N	C00O	C00K	119.90(17)

Table S5. Details of the best possible interaction of ligands (**L1-L3**) with the protein EGFR (PDB id.1M17).

Ligand	Binding energy	Kd	LE	Interaction	Distance	Category	Binding type
L1	-8.6	4.94 X 10^{-07}	-0.34	N_2H - ASP831	2.93526	Hydrogen Bond	Conventional
				ASP831 - π (C_{15}- C_{18})	3.45517	Electrostatic	Pi-Anion
				ASP831 - π (C_{15}- C_{18})	3.8979	Electrostatic	Pi-Anion
				PHE699 - π (C_{15}- C_{18})	3.82359	Hydrophobic	Pi-Pi Stacked
				Cl_2 - LEU694	4.3379	Hydrophobic	Alkyl
				Cl_2- LEU768	4.6251	Hydrophobic	Alkyl
				Cl_1 - LYS721	4.48468	Hydrophobic	Alkyl
				Cl_1 - MET742	4.78088	Hydrophobic	Alkyl
				Cl_1 - LEU764	4.69164	Hydrophobic	Alkyl
				π (C_8- C_{13}) - LEU694	5.06016	Hydrophobic	Pi-Alkyl
				π (C_8- C_{13}) - VAL702	5.25578	Hydrophobic	Pi-Alkyl
				π (C_8- C_{13}) - ALA719	4.88438	Hydrophobic	Pi-Alkyl
				π (C_8- C_{13}) - LEU820	4.88408	Hydrophobic	Pi-Alkyl
				π (C_2- C_7) - VAL702	5.00685	Hydrophobic	Pi-Alkyl
				π (C_2- C_7) - LYS721	4.71338	Hydrophobic	Pi-Alkyl
L2	-8.4	6.92 X 10^{-07}	-0.35	ASP831HN1 - N_3	2.7256	Hydrogen Bond	Conventional
				π (C_{15}- C_{18}) - GLU738OE2	3.42274	Hydrogen Bond	Carbon Hydrogen
				LYS721 - π (C_{15}- C_{18})	4.80847	Electrostatic	Pi-Cation
				LEU694 - π (C_2- C_7)	3.43971	Hydrophobic	Pi-Sigma
				MET742 - π (C_{15}- C_{18})	4.78711	Other	Pi-Sulfur
				CYS751 - π (C_{15}- C_{18})	4.39079	Other	Pi-Sulfur
				Cl - LEU694	4.42598	Hydrophobic	Alkyl
				π (C_8- C_{13}) - VAL702	4.95084	Hydrophobic	Pi-Alkyl
L3	-8.7	4.17 X 10^{-07}	-0.36	CYS773 - N_5	2.34672	Hydrogen Bond	Conventional
				N_2H - THR830	2.09009	Hydrogen Bond	Conventional
				LYS721 - π (C_2- C_7)	4.62819	Electrostatic	Pi-Cation
				LEU820 - π (C_8- C_{13})	3.83682	Hydrophobic	Pi-Sigma
				MET742 - π (C_2- C_7)	5.16157	Other	Pi-Sulfur
				π (C_{15}- C_{18}) - CYS773	4.02175	Hydrophobic	Pi-Alkyl
				π (C_2- C_7) - LYS721	4.11656	Hydrophobic	Pi-Alkyl
				π (C_8- C_{13}) - VAL702	5.47147	Hydrophobic	Pi-Alkyl
				π (C_8- C_{13}) - ALA719	3.50188	Hydrophobic	Pi-Alkyl

Table S6. Details of the best possible interaction of ligands (**L1-L3**) with the protein PI3Kα (PDB id. 4JPS).

Ligand	Binding energy	Kd	LE	Interaction	Distance	category	binding type
L1	-8.2	9.7 X 10^{-07}	-0.33	ASN465 - N_3	1.98345	Hydrogen Bond	Conventional
				GLN478 – O	2.06737	Hydrogen Bond	Conventional
				ASN467 - π (C_{15}- C_{18})	2.14797	Hydrogen Bond	Pi-Donor
				Cl_2 - PRO3	4.61141	Hydrophobic	Alkyl
				π (C_{15}- C_{18}) - PRO447	4.75937	Hydrophobic	Pi-Alkyl

				π (C_2- C_7) - LYS678	5.45106	Hydrophobic	Pi-Alkyl
L2	-8.5	5.85 X 10^{-07}	-0.35	ARG4 - N_4	2.29103	Hydrogen Bond	Conventional
				LYS672 - N_3	2.30754	Hydrogen Bond	Conventional
				GLU710 - π (C_{15}- C_{18})	3.58865	Electrostatic	Pi-Anion
				HIS676 - π (C_8- C_{13})	5.65585	Hydrophobic	Pi-Pi T-shaped
				π (C_{15}- C_{18})- ARG4	5.08992	Hydrophobic	Pi-Alkyl
				π (C_2- C_7)- PRO3	5.29732	Hydrophobic	Pi-Alkyl
L3	-8.6	4.94 X 10^{-07}	-0.36	ARG818 - N_2	2.85328	Hydrogen Bond	Conventional
				ARG818 - N_5	3.48608	Hydrogen Bond	Carbon Hydrogen
				LYS271 - π (C_{15}- C_{18})	3.16118	Hydrogen Bond; Electrostatic	Pi-Cation; Hydrogen Bond
				ARG818 - π (C_{15}- C_{18})	3.33748	Electrostatic	Pi-Cation
				ARG818 - π (C_2- C_7)	4.25433	Electrostatic	Pi-Cation
				PHE666 - π (C_2- C_7)	4.1312	Hydrophobic	Pi-Pi Stacked
				π (C_{15}- C_{18}) - LYS271	4.74523	Hydrophobic	Pi-Alkyl

Table S7. Details of the best possible interaction of ligands (**L1-L3**) with the protein Bcl-2 (PDB id. 4LXD).

Ligand	Binding energy	Kd	LE	Interaction	Distance	category	binding type
L1	-8.9	2.97 X 10^{-07}	-0.36	C_{16} - ASP108	3.50277	Hydrogen Bond	Carbon Hydrogen Bond
				C_{17} - GLN115	3.6423	Hydrogen Bond	Carbon Hydrogen Bond
				MET112 - π (C_{15}- C_{18})	3.56722	Hydrophobic	Pi-Sigma
				MET112 - π (C_{15}- C_{18})	4.46476	Other	Pi-Sulfur
				PHE101 - π (C_2- C_7)	4.87914	Hydrophobic	Pi-Pi T-shaped
				PHE101 - π (C_8- C_{13})	4.72506	Hydrophobic	Pi-Pi T-shaped
				TYR105 - π (C_8- C_{13})	4.79335	Hydrophobic	Pi-Pi T-shaped
				Cl_1 - VAL153	4.37559	Hydrophobic	Alkyl
				TYR105 - Cl_2	4.54451	Hydrophobic	Pi-Alkyl
				PHE109 - Cl_1	4.89298	Hydrophobic	Pi-Alkyl
				π (C_2- C_7) - ALA146	5.07385	Hydrophobic	Pi-Alkyl
				π (C_8- C_{13}) - ALA146	4.64107	Hydrophobic	Pi-Alkyl
L2	-8.6	4.94 X 10^{-07}	-0.36	C_{16} - GLU133	3.5143	Hydrogen Bond	Carbon Hydrogen Bond
				PHE101 - π (C_2- C_7)	4.9176	Hydrophobic	Pi-Pi T-shaped
				PHE101 - π (C_8- C_{13})	4.77564	Hydrophobic	Pi-Pi T-shaped
				TYR105 - π (C_8- C_{13})	4.77588	Hydrophobic	Pi-Pi T-shaped
				Cl - MET112	4.95282	Hydrophobic	Alkyl
				Cl - VAL153	4.50746	Hydrophobic	Alkyl
				PHE109 – Cl	5.27841	Hydrophobic	Pi-Alkyl
				π (C_2- C_7) - ALA146	4.55867	Hydrophobic	Pi-Alkyl
				π (C_8- C_{13})- ALA146	4.59816	Hydrophobic	Pi-Alkyl
L3	-8.1	11.5 X 10^{-07}	-0.34	GLU133 - π (C_{15}- C_{18})	3.40619	Electrostatic	Pi-Anion
				PHE101 - π (C_2- C_7)	4.88949	Hydrophobic	Pi-Pi T-shaped
				PHE101 - π (C_8- C_{13})	4.66203	Hydrophobic	Pi-Pi T-shaped
				TYR105 - π (C_8- C_{13})	4.89117	Hydrophobic	Pi-Pi T-shaped
				π (C_2- C_7) - ALA146	4.99968	Hydrophobic	Pi-Alkyl
				π (C_8- C_{13})- ALA146	4.60205	Hydrophobic	Pi-Alkyl